Revisiting regional and seasonal variations in decadal carbon monoxide variability: Global reversal of growth rate

Ankit Patel[1,a], Chinmay Mallik[1], Naveen Chandra[2], Prabir K. Patra[2,3], Martin Steinbacher[4].

1. Department of Atmospheric Science, Central University of Rajasthan, Ajmer, 305801, India

2. Research Institute for Global Change, JAMSTEC, Yokohama, 2360001, Japan

3. Research Institute for Humanity and Nature, Kyoto, Japan

4. Empa, Swiss Federal Laboratories for Materials Science and Technology, CH-8600 Duebendorf, Switzerland

[a] now at EE Division, Department of Civil Engineering, Indian Institute of Technology Madras, Chennai, India

Abstract

Carbon monoxide (CO) is one of the important trace gases in the atmosphere capturing the evolution of chemical properties of the troposphere. Here we analyze the growth rates of CO during the period of 1991 – 2020 using *in situ* measurements from the World Meteorological Organization's (WMO) Global Atmospheric Watch (GAW) program. The analysis of trends has been done on different spatial and temporal scales. Our analysis supports the decline in the overall CO mixing ratios over the globe but inter-decadal and regional trend analysis has shown heterogeneous changes in the given period of study. On average, there has been a decrease of -16.22 ± 1.92 ppb and -4.5 ± 0.64 ppb observed at the sites in the northern hemisphere (NH) and southern hemisphere (SH), respectively. This decline occurred at rates of -0.80 ± 0.12 ppb yr^{-1} in the NH and -0.12 ± 0.03 ppb yr^{-1} in the SH. Bifurcating the annual trends for seasonal analysis reveals the impact of emissions, chemistry and atmospheric transport on CO variation over different regional clusters of stations. Seasonal trend analysis

provides further evidence regarding heterogeneous patterns in the South-East Asia region. Our study highlights a slowdown in CO decline during the 2011-2020 decade when compared to the rate of decrease observed in 2001-2010. This is inferred from the variability and much slower decline of CO emissions across different regions, contributing to a weakening in CO trends.

Keywords: Carbon monoxide, trends, emissions, inter-decadal, regional trend analysis

1. Introduction

Carbon monoxide (CO) is not only an important toxic atmospheric pollutant but also a crucial player in regional and global atmospheric chemistry. In the radiation budget of Earth's atmosphere, CO has an indirect radiative forcing of +0.2 Wm^{-2} (Myhre et al., 2013). As a primary pollutant, it reduces the oxygen-carrying capacity of the blood, which can lead to unconsciousness and even death at high CO levels (WHO, 1999). The sources of CO are ubiquitous as it is formed during incomplete combustions of carbon-containing materials including fossil fuels in industry, transportation, residential combustion, burning of agricultural residues, and forest fires. About 2600 Tg CO is emitted per year globally, split between direct emissions and chemical production. The direct emission sources include anthropogenic (27%), biogenic (7%), and biomass burning (19%) while chemical sources include CH_4 oxidation (34.5%) and NMVOC oxidation (11.5%) (Zheng et al., 2019). It can be conceived that with increasing needs for food and fuel, the emission of CO will increase, particularly in developing regions of the world. The emissions can additionally lead to an increase in CO through the oxidation of hydrocarbons in the atmosphere. The overwhelming contribution of anthropogenic CO emissions in the Northern Hemisphere (NH) is responsible to maintain CO at a twice higher level in the NH than in the Southern Hemisphere (SH) and it

has grown in the latter part of the 20th century following the industrialization and population growth (Ehhalt and Prather, 2001). This is because the OH concentrations are suggested to be in parity between the hemispheres (Patra et al., 2014; Strode et al., 2015) and in the SH, CO is primarily emitted from biomass burning and as an oxidation byproduct of the volatile organic carbon (VOCs) (Gaubert et al., 2016; Lelieveld et al., 2016).

CO is a major sink (about 40%) for atmospheric OH radicals, the major cleansing agent of the atmosphere, at weekly-monthly time scales (Lelieveld et al., 2016). The oxidation of CO by OH (R1) has several implications for atmospheric chemistry including the HO_x cycling, the production of tropospheric ozone, and the lifetime of greenhouse gases like methane, hydrofluorocarbons (HFCs). In addition, CO changes has strong impact on coupled system of CO-OH-CH_4 chemistry in atmosphere. Lifetime of methane is very sensitive to the CO changes (Nguyen et al., 2020; Shindell et al., 2006). Increase in CO will lead to lower levels of OH in the atmosphere and cause increase in CH_4 lifetime and vice-versa (Ehhalt and Prather, 2001; Gaubert et al., 2017)

$$CO + OH + O_2 \rightarrow CO_2 + HO_2 \quad \text{R1}$$

CO constitutes a significant part of OH reactivity for low OH reactivity environments (Safieddine et al., 2017). In strong polluted air, NO_2 can also be a large OH sink through self-limiting reaction. NOx is an important contributor to atmospheric chemical cycling impacting both O_3 production as well as secondary OH production through recycling process. For a low NOx environment in Cyprus where OH could be successfully simulated within 10% of observations, it was observed that the OH recycling efficiency increased from 0.28 at 10 pptv of NO to 0.7 at 100 pptv of NO corresponding to a chain length of 2.8 (Mallik et al., 2018). The recycling efficiency peaked at 0.85 at 500 pptv of NO or about 3 ppbv of NOx after which it stabilized, meaning no additional efficiency of OH production at higher NO. This

76 situation may resemble relatively low anthropogenic emission regions of the world while at
77 higher emission regions, the NOx recycling mechanism of OH results in O_3 production
78 through photo-dissociation of NO_2 in presence of UV (Lelieveld et al., 2016). The reaction of
79 NO_2 with OH will be a direct competitor for the reaction of CO with OH as though CO-OH
80 rate constant is much slower; the CO has much higher concentration. The situation can be
81 analogous to the large CH_4 depletions observed in tropical regions with high atmospheric
82 H_2O concentrations and a strong formation of O_3 due to the NOx emissions (Rosanka et al.,
83 2020). While the global distribution of OH shows higher values between the tropics with
84 hotspots over equatorial rainforests (Lelieveld et al., 2016), high secondary OH formation is
85 observed over India and South-East Asia in addition to biogenically dominated rainforest
86 regions.
87 CO air samples collected by NOAA/CMDL revealed a significant long term downward CO
88 trend during 1990s that was largely confined to the NH. In SH, CO exhibits a considerable
89 interannual variability but the trend was insignificant (Novelli et al., 2003). A global decline
90 of 0.52 ± 0.10 ppb yr^{-1} between 1991-2001 was estimated with a steady decline of 0.92 ±
91 0.15 ppb yr^{-1} in NH. Various regional studies have mentioned a significant decline in CO
92 during mid 1990's and reported that changes were due to decrease in vehicular emissions in
93 Europe and USA. (Bradley et al., 1999; Hallock-Waters et al., 1999; Novelli et al., 1998).
94 ECHAM5/MESSy, an atmospheric chemistry GCM simulated downward trend in NH as well
95 as in SH with decreasing rate of 13.5 ± 11.1 ppbv/decade and 0.8 ± 6.7 ppbv/decade
96 respectively with global decline of 7.2 ± 7.8 ppbv/decade during 2001-2010. Modeled surface
97 CO estimated a significant decrease in over northern Australia, eastern USA, western Europe
98 with rates of 13.7 ± 9.5, 59.6 ± 9.1, 35.5 ± 5.8 ppbv/decade, respectively. But in southern
99 Asia and eastern China, a positive CO trend of +8.9 ± 4.8 ppbv/decade and +9.1 ± 9.7
100 ppbv/decade was present, though not statistically significant (Yoon and Pozzer, 2014).

Tropospheric CO columns observed by MOPITT declined at an average rate of -0.32 ± 0.05 % yr^{-1} over the whole globe and is consistent with the negative trends at WDCGG network (60°N-60°S) during 2000–2017 (Deeter et al., 2015; Worden et al., 2013; Zheng et al., 2019). MOPITT, AIRS, TES and IASI measurements consistently showed a decrease in CO trends in NH and SH during 2000-2011 particularly over the regions with high population density (Worden et al., 2013). MOPITT showed decreasing trend of -1.4 ± 0.2 % yr^{-1} and 1.6 ± 0.5 % yr^{-1} over USA and China during 2000s. However, a spatial heterogenity existed with the largest decrease in northern mid latitudes (30°N–60°N) (Gaubert et al., 2017). The tropical region (30°S–30°N) has a smaller decrease in CO columns due to increasing trends existing over South Asia and a large part of Africa. However, such fire-prone regions could potentially counteract with global decline in CO by local changes in biomass burning especially in summer. Because of the large fire activities and interannual variabilities in sources, determining the CO trends is such regions is very difficult (Fanin and van der Werf, 2017; Strode and Pawson, 2013). Asia is the only region that has a statistically significant trend of rising CO columns since 2000 (Zheng et al., 2019). In the southern mid-latitudes (30°S–60°S), which are mostly covered by oceans and have limited landmasses, both MOPITT and WDCGG data consistently indicate a notable decline in CO levels (Zheng et al., 2019). Satellite observations are consistent in the negative trend with WDCGG sites during 2001-2015 which confirms the decrease in global tropospheric CO (Jiang et al., 2017; Warner et al., 2013). TIR-CO satellite records of 2002-2018 from MOPITT, AIRS, TES, IASI has shown a global slow-down to a reduced negative trend in recent years by comparing trends for 2002–2010 with 2010–2018 from -1 % per year to -0.50 (±0.3) % per year (Buchholz et al., 2021).

Due to its fairly long lifetime (weeks - months), CO emissions over a region can influence its zonal-mean mixing ratio levels. Since local CO emissions can quickly transcend to zonal scales, it is necessary to study a global network of stations to make inferences regarding factors influencing CO levels and growth rates over a location. Systematic ground-based observations of CO started in the late 1980s pioneered by NOAA's cooperative flask sampling network (Novelli et al., 1992; Novelli et al., 1998a).

Availability of long-term measurements of CO from several sites around the globe from the World Data Center for Greenhouse Gases (WDCGG) makes it a lucrative option to study global and regional CO growth rates. As CO levels in a location are impacted by local emissions, atmospheric transport as well as atmospheric photochemical process, deciphering the intricacies of CO trends has been a topic of much debate (Buchholz et al., 2021; Hedelius et al., 2021; Zheng et al., 2019) In the present study, we analyze the growth rates of CO during the period of 1991 – 2020 using data from ground-based *in situ* observations and flask samples retrieved from the WDCGG to unravel the heterogeneities in different regional, spatial and temporal scales.

2. Materials and methods

For the present study, 49 stations from an initial list of 129 stations of the WDCGG data archive were selected based on the data availability and location of the stations (Figure 1, Table 1). WDCGG is a World Data Centre operated by the Japan Meteorological Agency (JMA) under the Global Atmospheric Watch (GAW) program of the World Meteorological Organization (WMO) (https://gaw.kishou.go.jp/). CO sampling follows WMO recommendations and utilizes three methods: continuous in-situ observation, surface flask air sampling, and onboard ship-based (mobile) sampling (Crotwell et al., 2020; NOAA, 2018).

151 The stations in our study employ both in-situ and flask-based sampling (Table S1). Flask air
152 sampling collects discrete air samples in specialized flasks, analyzed centrally. NOAA and
153 CSIRO use glass flasks with Teflon (PTFE or PFA) with O-rings for long-term storage,
154 offering cost-effective CO data collection for monthly, seasonal, and inter-annual analysis.
155 Air samples are collected in metal and glass flasks, carefully considering materials, protocols,
156 and storage conditions to minimize contamination. Weekly sampling ensures data quality and
157 trend analysis. *In situ* continuous observations provide near-real-time data with a temporal
158 range from seconds to one hour. For precise CO measurements, various techniques are
159 employed, including NDIR, GC/FID, GC/HgO, and VURF, which can detect fast changes in
160 the mole fractions (Zellweger et al., 2009). These techniques exhibit overall agreement better
161 than 2% for 1-hourly averages. Each technique has unique advantages and limitations; NDIR
162 offers robustness, GC/HgO has low detection limits, VURF provides high-frequency
163 measurements, and GC/FID simultaneously detects additional greenhouse gases like CO_2 and
164 CH_4, enriching the QA/QC framework to cover various environmental scenarios. VURF,
165 based on resonance CO fluorescence in the vacuum ultraviolet, excels in accuracy and low
166 detection limits (Gerbig et al., 1999). The data processing involves automated quality control
167 and manual review. It aims to create a time series of mole fractions representing ambient
168 conditions, while flagging artifacts. No entries are removed; instead, non-representative
169 samples are flagged. Flags stem from calibration and instrument issues, to outlier detection
170 (via sophisticated curve fitting). High-resolution CO data are aggregated into hourly, daily,
171 weekly, and monthly averages for analysis (WMO-GAW, 2010)./
172
173 For the atmospheric transport of CO using wind vector analysis, reanalysis data of global
174 wind was collected from NOAA (https://psl.noaa.gov). Anthropogenic emissions of CO from
175 different sources are taken from EDGAR-v6.0 inventory

(https://edgar.jrc.ec.europa.eu/dataset_ghg60) (Crippa et al., 2021). The ENSO Index time series was taken from Multivariate ENSO Index Version 2 (MEI.v2) provided by the Physical Sciences Division of the Earth System Research Laboratory of the National Oceanic and Atmospheric Administration (NOAA). (NOAA, 2020) (https://www.psl.noaa.gov/enso/mei/)

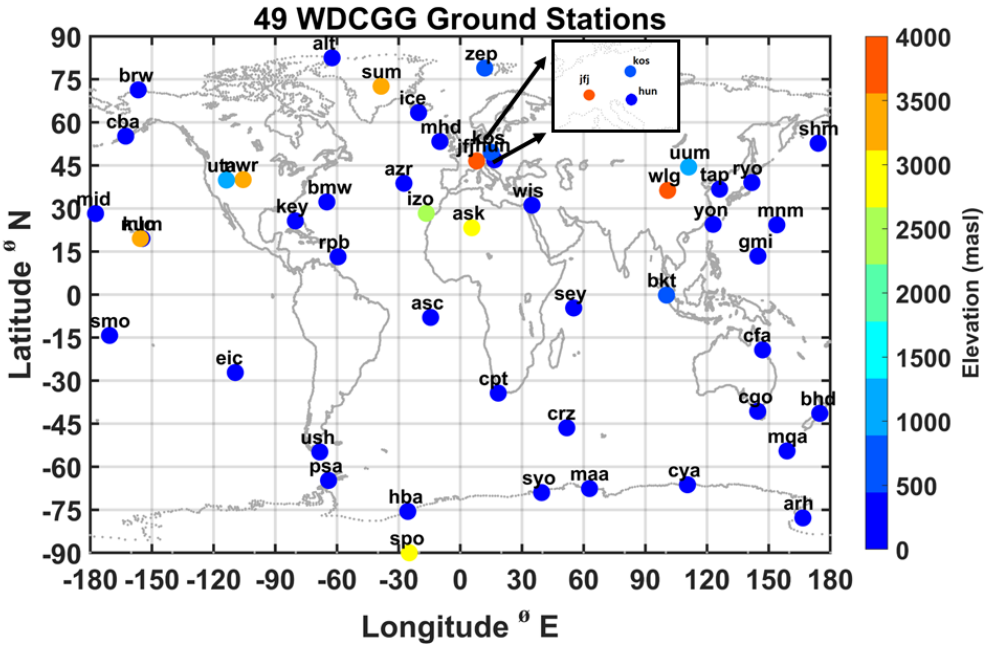

Figure 1. Spatial coverage of stations selected for this analysis from the WDCGG database (http://ds.data.jma.go.jp/gmd/wdcgg/). See Table S1 for other details of stations.

The WDCGG data repository hosts hourly, daily, event, and monthly datasets. For the given study, monthly data have been used. The monthly datasets had continuous time series of CO with some data gaps for a few sites. To fill these missing monthly data points in such case a simple linear interpolation is not an adequate approach and, a curve-fitting procedure was applied. The digital filtering (DF) and curve fitting technique was developed at Tohoku University (Nakazawa et al., 1997a), which has been used for various flask measurements in the past for long term-trend determination (Chandra et al., 2022; Patra et al., 2005; Yashiro et

al., 2009).. Digital filtering is a statistical procedure that uses Fourier harmonics, Reinsch-type cubic splines, linear interpolation, and a Butterworth filter to approximate the long-term temporal trends, seasonal cycles, and growth rate. The processes primarily involve the following four steps: (i) approximation of seasonal cycle and long-term trend, (ii) extrapolation and interpolation of the data, (iii) calculation of the seasonal cycle and long-term trend on average, and (iv) extraction of the seasonal cycle and interannual variations. To determine the long-term trend and curve fitting each data point was fitted individually using the Butterworth filter with a cut-off duration of 48 months and 3 harmonics (sinusoidal form of a Fourier function) in this technique. Unevenly spaced initial data is first detrended and then seasonal cycles are removed by fitting smoothing spline & Fourier components of data. The residuals were then interpolated onto evenly spaced data format followed by passing it through the Butterworth filter. Outliers, defined as data larger than 3 standard errors away from the fitted curve, were successively rejected after each iterative fit. More detailed information about the DF technique can be found in (Hung et al., 2005; Nakazawa et al., 1997a; Pickers and Manning, 2015). The fitted curve of the DF method generally exhibits a good representation of sharp temporal variation in mixing ratios without erroneous ripples. After applying DF on the raw monthly dataset of 1991-2020, a smooth fitted continuous time series data with no gaps was generated for each station. The availability of final monthly data is shown in Figure 2. This smoothed fitted monthly dataset was then used for the trend analysis. Then the Mann-Kendall test and Theil-Sen estimator were used to conduct a trend analysis on the monthly averaged time series. Mann-Kendall test is a statistical tool to check whether the time series has decreasing, increasing or no trends. And if a trend is present, the Theil-Sen estimator or Sen's Slope technique was used to calculate the slope of the trend (Li et al., 2022). The Theil-Sen method is a robust linear regression method widely used for trendline's slope estimation. It competes effectively with simple linear regression and the

simple least squares methods and is an efficient and commonly used nonparametric method of estimating a linear trend (Jindal et al., 2020; Kamal and Pachauri, 2019).

The data from the majority of stations comes from flask-based sampling. Although the sampling is designed to sample background air, local influences cannot be entirely ruled out and sporadic polluted samples can sometimes bias the monthly mean values. About 83.7 % of the stations have more than 25 years of data while 14.3 % of stations have data between 20-25 years. Only 1 station out of 49 have comparatively less data e.g., 'bkt' in Indonesia have less than 20 years of data, but these sites are retained in our analysis due to their strategic location. To compute the long-term decadal trends, the 2/3 rule was strictly followed, i.e., at least 67% of data (7 years) in each decade must be present for decadal trend calculation.

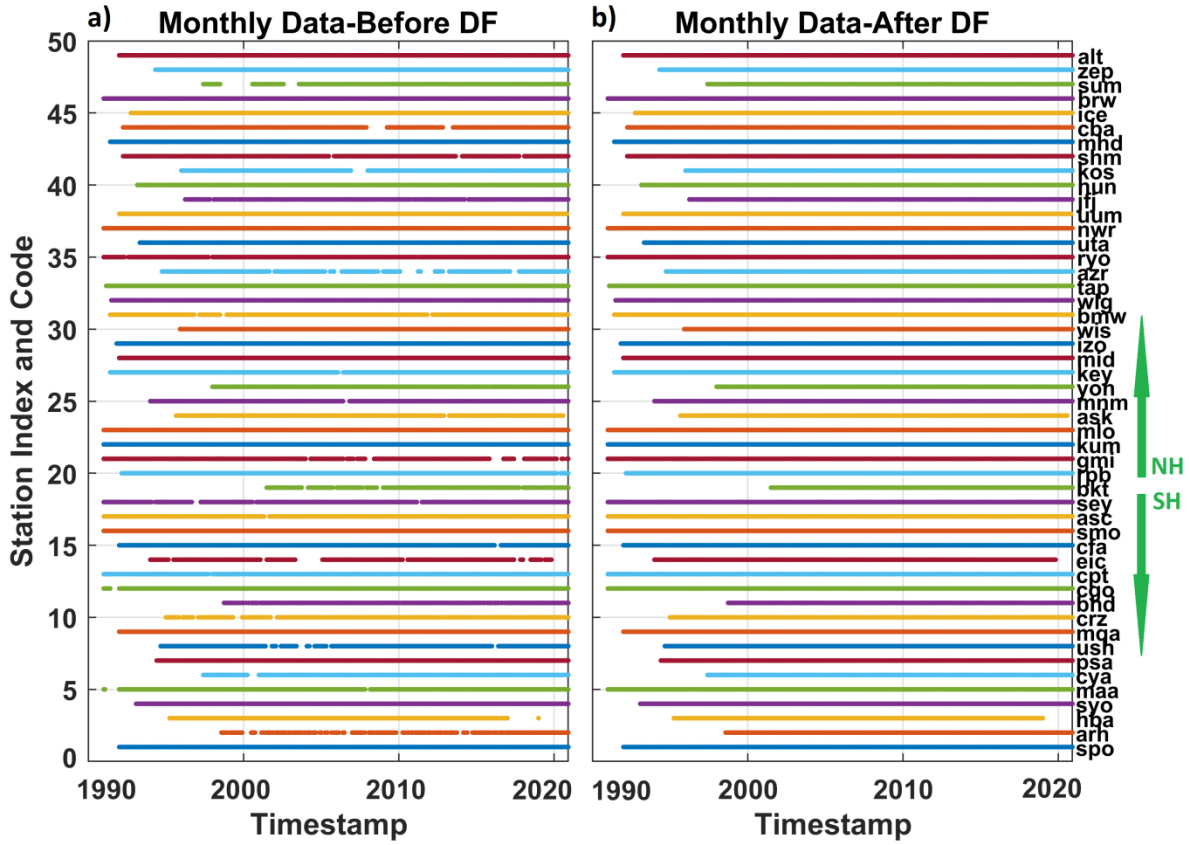

Figure 2. Data coverage for each site selected for this analysis from the WDCGG database (http://ds.data.jma.go.jp/gmd/wdcgg/). The left panel is the data availability of original

monthly dataset having some missing data points for a few sites. The right panel is the final monthly data availability after curve fitting.

3. Results and discussion

3.1. Global CO levels, variability, and trends: General features

Out of the 49 stations analyzed during this study, a decrease in CO levels is observed for 45 stations, and these trends were further classified into statistical significance categories. Specifically, 38 stations exhibited a statistically significant decrease, with a level of significance at 0.05 under The Theil-Sen method, while the remaining 11 stations showed a slightly positive trend (Figure 3). There is an overall declining trend in CO in the last 3 decades. Stations having significant and non-significant CO trends with p-values can be found in Figure S1. There are few sites like 'bkt' with insignificant confidence interval. However, these sites are kept in the analysis for their critical location on the global scale. The 'bkt' station on Western Sumatra is occasionally exposed to emissions from persistent biomass burning events. Thus, the calculated trend can be biased by the appearance and the strength of these events within the observed period (Figure S2). Over the past three decades, there has been a consistent decline in CO levels. While this global trend shows a general decrease in CO, it is important to note that there is significant spatial variation in the distribution of these trends.. Three out of 18 stations in SH have slight positive trends (increase rate less than 0.25 ppb yr^{-1}) and other stations show slight negative trends in CO (decrease rate less than 0.25 ppb yr^{-1}) whereas downtrends within NH stations are very contrasting.

The decreasing trends of CO could either be related to an increase in CO chemical loss rates or a decrease in both the CO primary emissions and chemical production. The CO loss (R1)

and it's chemical production involves OH, and their effects on CO mixing ratio are opposite. The loss rates of methyl chloroform (MCF), derived from the 12-month difference of monthly means in successive years, shows very small normalized variation (of the order of 0.2%) during 2001-2018 (Patra et al., 2021). This does not support the hypothesis that the CO decrease can be explained based on changes in global OH distributions alone (Jiang et al., 2017). Rather, the decrease in CO emissions is a more reasonable explanation for stronger decreasing trends of CO in the northern latitudes (>23.5˚N), relative to the sites in the latitudes south of this (Figure 1).

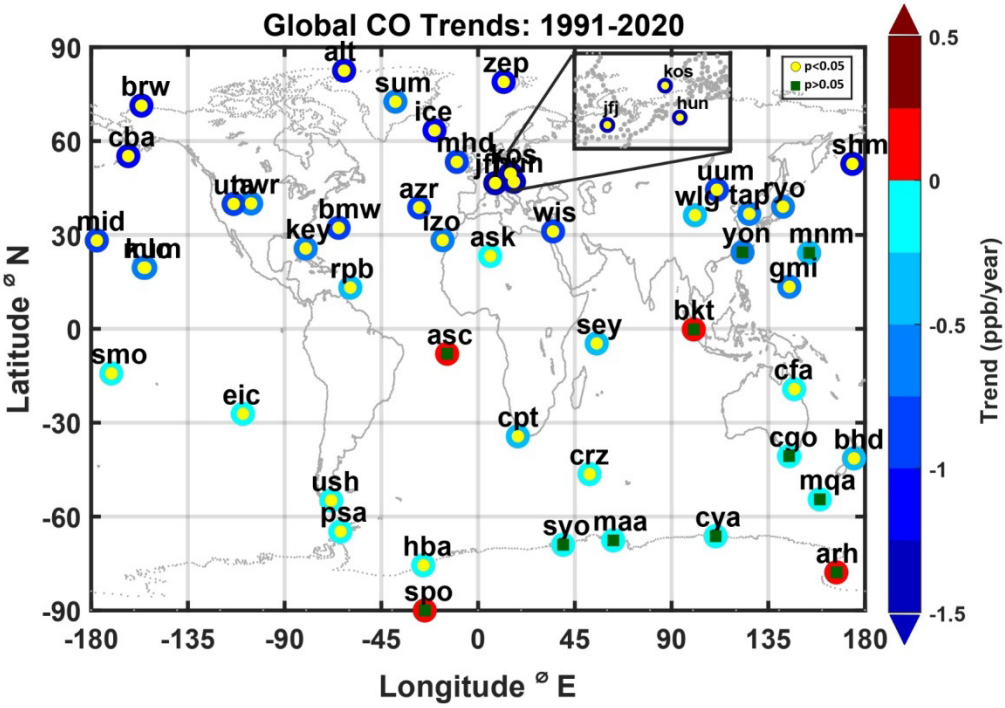

Figure 3. Spatial distribution of long-term trends in atmospheric CO during 1991-2020.

In the northern latitudes, all CO time series show negative trends for the 1991-2020 period (see Figure 3). Reduction in atmospheric CO levels was particularly recorded since 2003-2004 in agreement with the EDGAR anthropogenic emissions (Figure 4). Between 2000-2004, 22 sites out of 25 in this region have shown the highest growth rate in CO. This high growth rate was prominent between 50° N -70° N (sum, brw, ice, cba, mhd, shm) (Figure S4

A). Whereas some European sites (kos, hun, jfj) (Figure S4 B) have comparatively less growth rate during this period. However, over the tropics, the CO growth rates are not in sync with EDGAR emissions. East Asia shows high growth in emissions driven by energy use and industries; however, this is not reflected in mixing ratio trends in CO even over East Asian sites (Figure 3). For this zone, the average CO concentrations shows stabilization for most part of this century. Thus, an enhancement in CO from the EDGAR inventory emissions over East Asia (China, Hong Kong, Mongolia, Taiwan) and South Asia (India, Pakistan, Sri Lanka, Bangladesh) must be somewhat balanced by an increased CO chemical sink (OH) as observed for some stations in Figure S3.

Alternatively, reduced transport from higher latitudes may partly explain the stabilization. Moreover, the emissions from South Asia nations started increasing much later than the emissions from East-Asian countries (China, Hong Kong, Mongolia, Taiwan), suggesting a large influence of emissions from Chinese region on the tropical CO growth rates despite the fact that CO emissions by a major contributing sector (road transportation) have a decreasing slope after 2000s (Figure S5). However, the CO contribution from other sectors like industries, electricity-heat production, and solid fuels has increased unabated. South America is the major contributor to anthropogenic CO emissions (EDGARv6.0) in SH in all sectors except solid fuel while Southern Africa and Oceania (Australia, New Zealand, etc.) have contributed to a moderate increase in different sectors.

(Crippa et al., 2023) present HTAP_v3 MOSAIC CO emission data which shows a decline in Global CO emissions from 502.7 Mt to 499.8 Mt between 2000 – 2018. However, it has not been monotonically downwards but exhibits variability in regional trends (Crippa et al., 2016). Road transport accounted for the majority of CO emissions in the European Nations,

UK, USA and China and the development of emission standards contributed to a drastic reduction in total emissions (Guan et al., 2021; Oreggioni et al., 2022). Europe and North America, have shown reductions of -42% and -62%, respectively, in CO emissions. This is a consequence of implementing the EURO standards that have enabled specific emission reductions of up to 91% per unit of gasoline consumed which is a major contributor (Oreggioni et al., 2022). The combined effect of European policy and technological advances not only had significant positive effects on Europe itself but also significantly improved air quality in other regions of the world (Crippa et al., 2016; Kuklinska et al., 2015). CO emissions in Africa and South Asia have increased by 45% and 49%, respectively even though CO emissions from road transportation have reduced by 55% over the same period, while emissions from other sectors have increased (Crippa et al., 2023). These findings are consistent with (MOPITT) satellite retrievals, with similar patterns over different regions (Worden et al., 2013; Y Yin et al., 2015). MOZAIC-IAGOS measurements from commercial aircrafts (2001-2012) also showed a decline in CO in the NH along with a strong interhemispheric CO gradient in late winter/early spring (Osman et al., 2016).

Between 1985 and 2015, CO emissions from road transport significantly decreased by 93% in European nations and the UK, despite a 56% increase in total fuel consumption. This reduction is primarily attributed to the implementation of EURO standards, which achieved specific emission reductions of up to 91% per unit of gasoline consumed (Oreggioni et al., 2022). In ASEAN countries, this sector experienced the fastest growth during the same (Kurokawa et al., 2013). If controls, based on CHN-3 and CHN-4 standards, had not been enforced in China, CO emissions would have been 58% higher than the most recent data included in the EDGAR database (Oreggioni et al., 2022).

Based on EDGARv5 release, emissions from the energy and transport sectors significantly declined in the European Union, UK and USA between 1985 and 2015 and regions that are in the midst of industrialization, like China and other Southeast Asian nations, have witnessed exponential growths (M et al., 2021; Oreggioni et al., 2022). China experienced such growth in CO emissions between 1990 and 2005 due to rising demand, followed by relevant reductions. Since 2005, China's CO emissions have been decreasing due to improvements in energy efficiency and emission control laws (Guan et al., 2021; Xia et al., 2016). Among the available inventories, only the MEIC regional inventory for China aligns with the observed decrease in CO emissions as diagnosed through inversion methods. MEIC dataset shows that there is a cumulative decline of −32% from 2005 to 2016 and the decreasing CO emissions is driven by rapid technological changes with improved combustion efficiency and emission control measures in four main sectors (iron and steel industries, residential sources, gasoline-powered vehicles, and construction materials industries) in China. This led to 76% of the inversion-based trend of East Asian CO emissions. Global emission inventories underestimate the strength of emission control and recent reduction in CO emissions in China, which occurred despite the increased consumption of carbon-based fuel (Bo Zheng et al., 2018). Based on MEIC dataset, CO emissions increased from by +31% between 2000-2005 and then declined by –6% from 2006 to 2010 (Meng Li et al., 2017). Improvements in combustion efficiency, the recycling of industrial coal gases, and stringent car emission rules are all responsible for the decrease in CO emissions during 2006-2010 i.e. 11th FYP (M Li et al., 2017). CO emissions were falling by 1.2% year, which is in good agreement with many satellite datasets (Buchholz et al., 2021; Worden et al., 2013; Yumimoto et al., 2014). According to MEIC v1.2, CO emissions are down by 4% from 2011 to 2015, reaching a maximum reduction of 162 Tg. Due to the implementation of stringent vehicle emissions

standards, the share of transportation has decreased since 2006 (Buchholz et al., 2021; Meng Li et al., 2017).

Overall, CO growth rates calculated using WDCGG data are not in good agreement with emission inventories (e.g., EDGARv6.0), over the northern tropics and the southern hemisphere. The relatively stable CO concentration in the tropics could be a result of transport of decreasing CO from the NH extratropics (Figure 4a) and an increasing CO due to the increasing emissions within the tropics (Figure 4e). The emission increase in the SH is very small, at about 1 Gg yr^{-1} during 2005-2018 (Figure 4f), and the decrease in CO in the SH extratropics (Figure 4c) could be caused by the transport of airmass from the NH to SH through the upper troposphere (Belikov et al., 2022; Frederiksen and Francey, 2018).

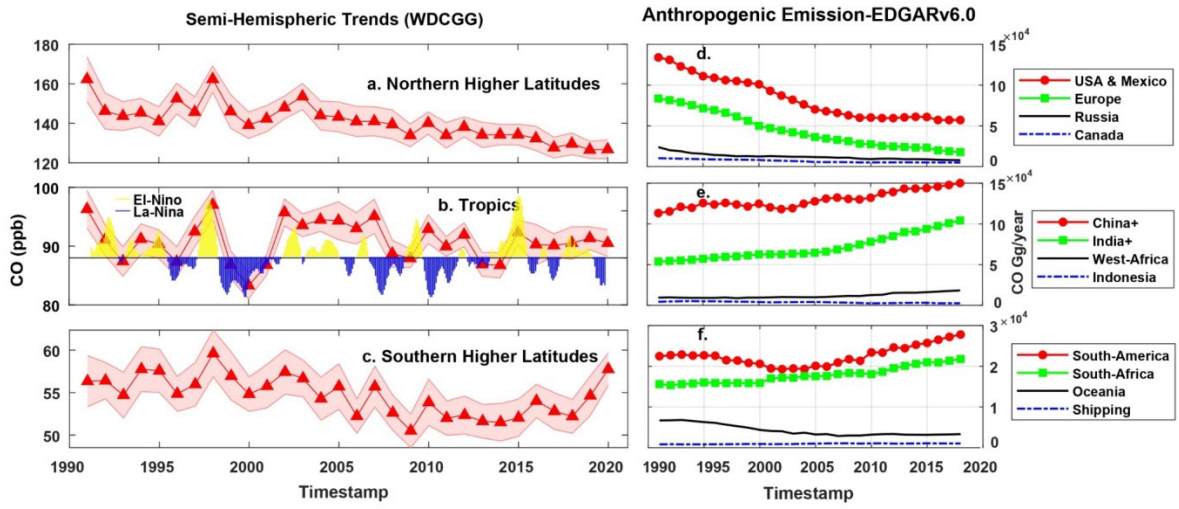

Figure 4. Time series of yearly averaged CO mixing ratios from WDCGG for the 3 broad latitude bands, of 75°N - 23.5°N, 23.5°N - 23.5°S, and 23.5°S - 75°S (panels a-c). The corresponding regional total CO emissions derived from EDGAR v6.0 are also shown (panels d-f). ENSO Index has shown (moderate La Nina: 2007-08, 2010-11; very strong El Nino: 1997-98, 2015-16; moderate El Nino: 2002-03, 2009-10, 2018-19).

3.2.Latitudinal variation and regional CO trends

366 The spatial heterogeneity in decreasing CO trends is addressed by looking into its spatial
367 distribution. Figures 4 and 5 show a clear distinction in CO mixing ratios between both
368 hemispheres. Mixing ratios were considerably higher in the Northern latitudes, especially in
369 the early years of the observations. Moreover, NH stations, especially between 15ºN-60ºN
370 have shown the strongest negative trends compared to other globally distributed sites. In this
371 latitudinal region, 18 out of 22 stations have shown very high seasonal CO mixing ratios
372 peaks varying between the range of 140-200 ppb having few sites (kos, hun, tap,) with more
373 than 250 ppb which is higher than the average global CO mixing ratio ~90 ppb as compared
374 to other sites in the NH. Also, these CO mixing ratio ranges are decreasing when moving
375 towards the Southern part of the globe. The difference in CO mixing ratio between the both
376 hemispheres is so high (average = 80-90 ppb) that the peak CO mixing ratio of sites between
377 15 ºS -90 ºS is below the minimum CO mixing ratio of most of NH sites. Despite
378 significantly higher mixing ratio in NH attributed to strong emission sources, the transport of
379 CO may not be able to reduce the N-S gradient significantly due to the short lifetime of CO.
380 Species with lifetime of about 1 year could be transported from one hemisphere to the other
381 (Belikov et al., 2022). The higher decreasing trends are observed in NH and become less
382 prominent towards the South. Figure 5 evinces a systematic distribution with negative trends
383 in the NH (<-0.5 ppb/year) and approaching the zero line with decreasing latitudes and close
384 to zero values from southern tropics to South Pole.
385
386 Apart from absolute values of trends, the variability of trends is higher in the NH compared
387 to the SH. The mean growth rate of CO is -0.87 ± 0.16 ppb/year ($p<0.01$) in the Northern
388 midlatitudes (23.5°N-66.5°N) while this value is -0.13 ± 0.04 ppb/year ($p<0.05$) in the
389 Southern midlatitudes. The tropical regions of the NH show a growth rate of –0.57 ± 0.08
390 ppb/year ($p<0.01$) in the 0-23.5°N while the rate is -0.15 ± 0.04 ppb/year ($p<0.01$) in the 0-

23.5°S. The latitudinal distribution of CO not only depends on the primary emissions but is also controlled via chemical production through oxidation of CH_4 by OH and chemical oxidative losses (Tie et al., 1992). Thus, the latitudinal distribution of OH will also exert a control on the photochemical production of CO.

Apart from the magnitude of OH and OH recycling probability, the trends in OH must be known to interpret their impacts on CO trends. To understand the relationship between CO and OH, the observed CO is compared to OH provided by TCR-2 (Tropospheric Chemistry Reanalysis version 2) (Miyazaki et al., 2020). Results are shown for a few example stations in Figure S3. For many stations like bhd, gmi, mnm and even to some extent 'yon', CO and OH are anti-correlated and a long-term decline in CO is accompanied by a long-term increase in OH indicating the important of atmospheric chemical mechanisms in controlling CO losses. Interestingly, unlike stations in Pacific where anti-correlation is clearly observed, in 'tap' at Korea directly experiencing humungous outflow of pollution from China, the trends in both CO and OH are negligible and run parallel to each other.

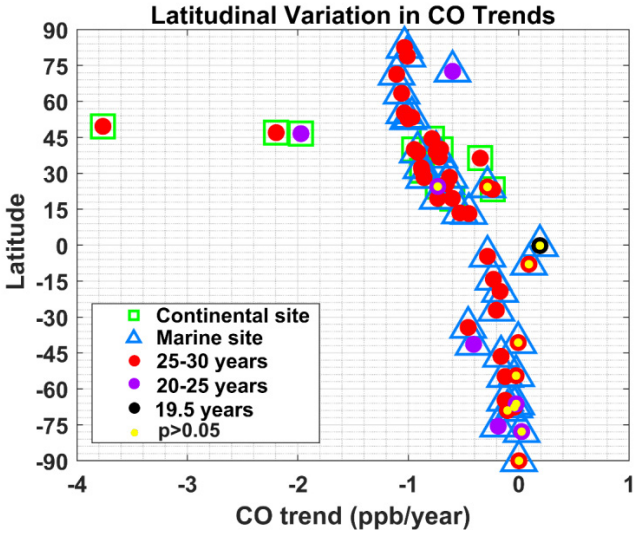

Figure 5. Latitudinal gradient of CO trends as observed at 49 sites. A dominancy of NH sites is observed latitudinally, with continental sites (□-marker) contributing higher CO (ppb) than the sites with marine background (Δ-marker). The colored circle inside each marker provides the information of the length of time series data (in years) available for each site.

To address the spatial heterogeneity in global CO trends, we conducted an in-depth analysis of regional trends. 5 groups were identified using weighted k-mean cluster analysis based on long-term trend, latitude, and longitude values with assigned weights of 16.6%, 33.3% and 50% respectively. (Figure 6). This method partitions N observations into k number of clusters based on the weight of input data. The trend values show largest variability (~ -0.23 to -3.7 ppb/year) in Cluster 1 with an average value of -1.05 ppb/year (Figure 6) and lowest variability (0 to -0.4 ppb/year) in the Australia region (Cluster 5, Figure 6). This is because Cluster 1 has a larger number of stations (14) as compared to other clusters and spans a large geographical area (European and East-American regions). These regions have mostly been regulated by emission control protocols as evident in the emission estimates in Figure 4 indicating reduced emissions could be responsible for the large negative trends as there is reduction in anthropogenic emission in industries, road-transportation etc. (EDGARv6.0). Data collected from the website of the International Energy Agency (https://www.iea.org/) also correlates with the fact that coal fuel consumption has been drastically reduced since 1990s in Europe. Lower variability is also observed for cluster 2 (0.09 to -0.46 ppb/year) while clusters 4 (0.1 to -1.0 ppb/year) and cluster 3 show intermediate variability (-0.2 to -1.1 ppb/year). The increasing strength and frequency of El-Nino events rather than the increase in fire events in the 2010-2020 period is likely to be responsible for the flipping of the CO growth curve from expected lines during 2015-2020 (Figure S2). ENSO can modulate the interdecadal CO growth rates in case more La Ninas in 2001-2010 produced a +ve (positive)

OH anomaly (negative CO growth rate), while more El Ninos in 2011-2020 produced -ve (negative) OH anomaly and positive CO growth rate. La Nina / El Nino also modulate the strength and the appearance of biomass burning. The El-Nino effect is also observed for other stations e.g. maa and mqa in the SH (Figure S6). Cluster 3 and 4 are dominated by emissions from China and stations located in East-Pacific region. Cluster 4 representing emissions over South-East Asian region shows high CO mixing ratios but low magnitude in annual negative trends. Despite having similar ranges because CO is relatively well mixed zonally (Figure 6), these trends are further decoupled into decadal and seasonal components to understand their variability.

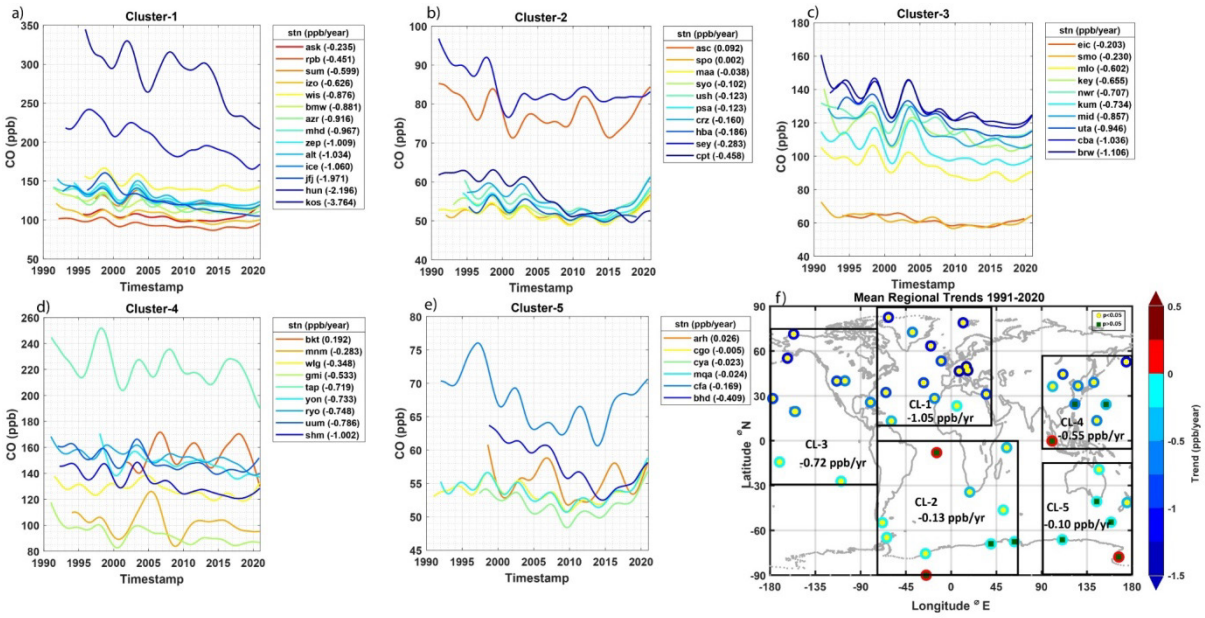

Figure 6. 5 regional clusters representing average CO trend of in respective region. Each cluster is grouped according on the closeness to centroid value of long-term trend, latitude and longitude. Right corner panel is a visual representation of each cluster on global map marked with average CO trend in respective cluster. Each panel of clusters has a de-seasonalized CO time series colored with respective trend values. A set of European + North Atlantic sites; Cluster-1 shows most negative trends of all groups and contributing more to

449 negative trends in NH. Each cluster differs in average CO ranges and magnitude of trend
450 slope (ppb/yr).
451
452 Biomass burning is a common source for both NOx and CO. Coincidentally, some of these
453 regions have also exhibited a strong positive trend in NOx e.g. over India (+29 %/decade),
454 China (+26 %/decade) based on surface emissions (Miyazaki et al., 2017). It was also
455 observed that tropospheric NO_2 showed an enhancement over China (40%), India (25%) and
456 SE Asia (13%) during 2005-2014 (Miyazaki et al., 2017). Negative trends were also observed
457 over several places in USA and Europe with larger negative trends during 2005–2010 than
458 2011–2014 while negative trend in NOx over China was observed after 2011. The same
459 analysis beautifully shows a correspondence between OH and NOx changes over many
460 places of the world using an approach to constrain the interdependent chemistry of CO and
461 NOx thorough O_3 and OH. Thus, changes in CO are not independent of NOx emissions due
462 to common constraining OH chemistry and if instances of large CO emissions like biomass
463 burning plumes are also accompanied by large NOx emissions, the oxidation chemistry may
464 be directly dependent on the recycling efficiency. In fact (Lelieveld et al., 2004) describe the
465 limiting nature of NOx on OH recycling and O_3 formation and point to a decrease in CO
466 concentration in NH along with an increase in NOx emissions in Asia.
467
468 A large fraction of CO variability is associated with ENSO and they vary by region to region,
469 e.g., as shown in Fig. 4. Interannual variability in upper tropospheric CO peaks in Southern
470 Hemisphere was observed using aircraft observations with enhanced values during strong El
471 Nino years e.g. 1997 (Matsueda et al, 1997). Although the CO peak in the SH high latitudes
472 in 2019-2020 (Fig. 4c) could be caused by the large Australian bush fires (Canadell et al.,
473 2021; Yang et al., 2021), GFAS fire emission flux shows a decreasing trend in most of the

region in last two decades (Fan et al., 2023). Also, a 25 % global decline has been observed in burned area and fire emissions between 1997-2015 and the area of global grassland fires generally shows a downward trend, except for parts of the Australia (Yin et al., 2020). The relative changes in burned area in Australia are highest suggesting that the fire occurred frequently with high intensity(Ohneiser et al., 2022; Yang et al., 2021) However, there exists a large interannual variations in the previous years (Chen et al., 2023; Fan et al., 2023). Those cannot be explained by the ENSO cycle, which we show to have a compact relation with CO variation in the tropics (Fig. 4b). Overall, variability and trends in vegetation fires vary strongly from continent to continent, as summarized by (Bowman et al., 2020). While Africa features a consistent decline in vegetation fire emissions (see also (Jiang et al., 2020)), fire emissions increased in the last decades especially in Brazilian Amazonia and the Western United States. In fact, in recent years, fire emissions during summer had increased whereas in winter it had decreased, therefore there has not been a major shift in the multi-year average emissions (Fan et al., 2023). Tagged CO experiments with CHASER model using data from container ships has revealed impact of forest fires and biomass burning on CO (Yashiro et al., 2009). A review by (Bowman et al., 2020) of studies looking into future projections of fire activity does not reveal a consistent pattern (i.e., either no change, mixed results or increase in fire activity). However, it does not report a decrease in fire activity in the future either.

Decadal variations in CO trends

To get an insight into the temporal evolution of CO trends, the analysis period of 1991-2020 has bifurcated into three decades: 1991-2000, 2001-2010 and 2011-2020. From this point forward, these decades will be referred to as the 1990s, 2000s, and 2010s, respectively. It must be noted that there are few sites having less data than 7 years between 1991-2000 (e.g., ask, crz). Decadal trends (1991-2000) of such sites are not calculated and not compared as 1991 vs 2000. Since these sites have continuous data after 2000, so comparison of these sites

499 can be seen in 2000s vs 2010s. These decadal trends shown in Figure 7 present a riveting
500 picture. The general downward trend in CO is not consistent for the whole period. The
501 number of sites with positive trend keeps increasing in each decade i.e., 7 sites in 1990s to 20
502 sites 2010s which is mainly noticeable in SH otherwise negative trends are constant to the
503 north of 20°N in each decade. The CO mixing ratios in the NH remains rather constant in the
504 1990, followed by a decrease till now. For SH, there is slight decrease observed from the
505 beginning but a leveling-off after 2010.The positive trend during 1990s for SH sites could be
506 influenced by a strong El Nino effect in the late 1990s, leading to increased biomass burning
507 contributions to CO. It may also indicate a reduction in strength of OH mediated chemical
508 loss of CO. It may be noted that the regions of high OH reactivity as well as OH recycling
509 probability lie in the SH (Lelieveld et al., 2016). So, a strong biomass burning event can
510 quickly disturb the natural OH cycling by injecting copious amounts of hydrocarbons. Thus,
511 these events will not only lead to primary CO emissions into the atmosphere but also change
512 the strength of chemical losses. Figure S3 for bkt shows simultaneous changes in observed
513 CO and modeled OH. It is very interesting to observe that normally the peaks in CO coincide
514 with the trough in OH. However, around 2013, the peaks in CO and OH are in sync, both
515 showing simultaneous enhancement along with strong biomass burning emissions (Figure
516 S3). The sync is also somewhat observed during 2017. Studies in 1990s pointed out that
517 emissions of CO and CH4 by biomass burning can affect the oxidation efficiency of the
518 atmosphere by scavenging hydroxyl radicals (Crutzen and Andreae, 1990). However, with
519 advancement in measurement techniques and detection of larges suites of non-methane
520 organic gases (NMOGs), biomass burning plumes, despite their importance, have mystified
521 our understanding as represented by contrasting characteristics in O_3 enhancement ratios
522 ($\Delta O_3/\Delta CO$) which has been shown to increase, decrease as well as remain unchanged
523 (Coggon et al., 2019) depending on NMOG/NOx ratios, downwind meteorology, and

incident solar radiation. This indicates that a systematic relation (sync or anti) in BB emission regions between CO and OH can be very quickly perturbed. (Müller et al., 2016) investigated temporal evolution of BB plumes from its origin to several kilometers downwind using high precision measurements along with a photochemical box model and found stable OH radical concentrations of 7.45 ± 1.07 × 106 cm−3 along a 13 km transect and NMOGs with more than 10 carbon atoms were found to be absent at mixing ratios larger than 50 pptv/ppmv CO emitted. Several studies have shown an enhancement in oxidation capacity of the atmosphere and hence OH formation during biomass burning and found a correlation between the interannual variation in O_3 and burned area (Zhu et al., 2021). While O_3 formation was found to be mainly limited by the availability of NOx, depending on the fuel nitrogen content and the combustion efficiency (Jaffe and Wigder, 2012), an efficient HO_2 regeneration was also observed (Alvarado et al., 2015). The HO2 regeneration can increase the OH levels through recycling while CO levels can be enhanced through oxidation of carbon compounds changing the OH-CO relationship from anti to sync and vice versa through high OH reactivity of a plethora of C compounds. The biomass burning net influence in South-East Asia was found to be large at 50% for OH, 40% for HO_2, 60% for HCHO, and 10 ppbv for O_3 along with an enhancement of CO. While on one hand, the OH decrease due to BB influence can be upto 40% in downwind regions below 1 km altitude, the BB nonradiative influence on OH becomes positive and can enhance OH concentrations by up to 90% (Tang et al., 2003).

Interesting, in the 2000s, most of these positive trends in SH had turned into negative. Going by the previous logic, the El-Nino events towards end of the 2000s decade were weaker. Under unstressed conditions, OH is mostly well-buffered and recycling would restore OH levels and the loss mechanisms will operate smoothly (Lelieveld et al., 2016; Mallik et al., 2018). Most of the European stations have continued their overall decreasing trend from

549 1990s into the 2000s. Interestingly, the negative trends over Korea during the 1990s have
550 turned into positive (although very close to zero) during the 2000s. Although along with
551 developed regions of the world in USA and Europe, most of the stations in East Asia also
552 continued with negative trends (Table S1, Figure 7). The tropical regions around Africa and
553 Asia have also shown positive trends in the 2000s, dominated by biomass burning effects
554 (Figure 4). The positive trends at 'tap' is consistent with other studies which says that the
555 trends at northeast Asia could potentially be effected by the changes in meteorology (Jiang et
556 al., 2017).

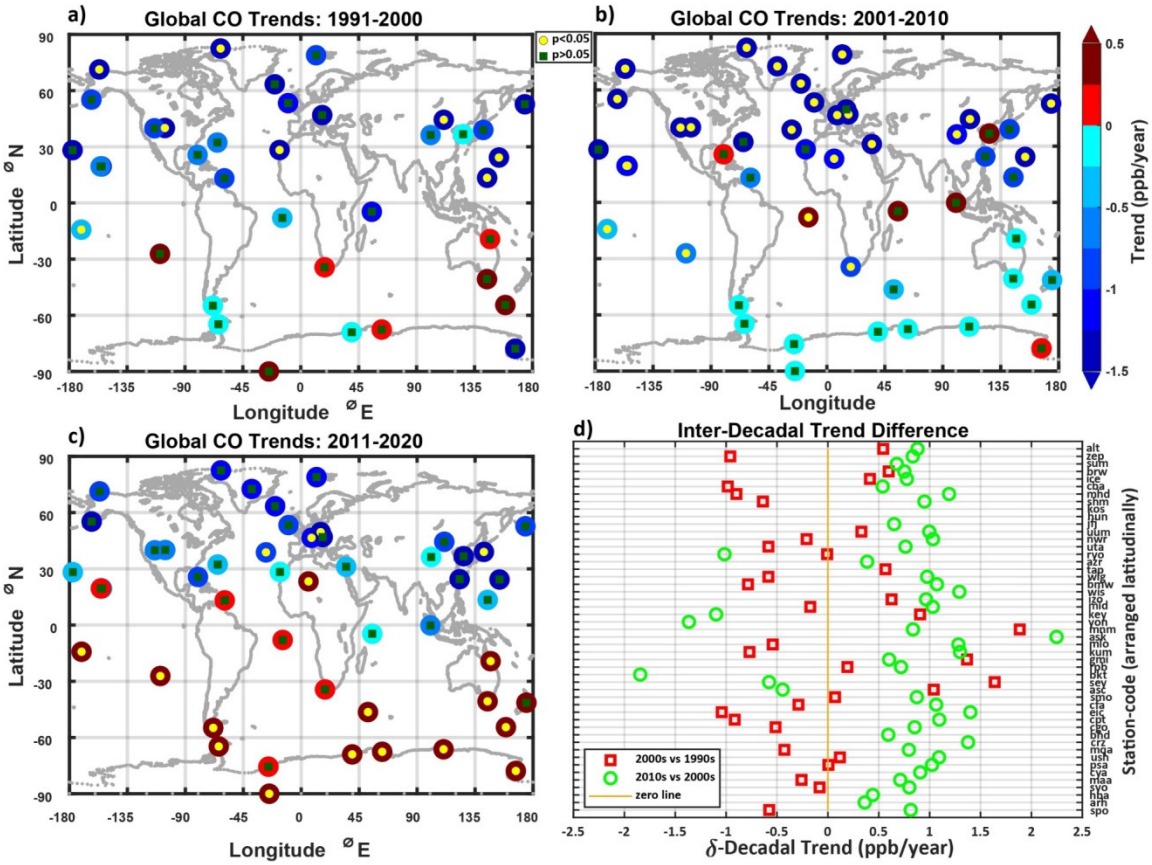

557

558

559 **Figure 7.** Decadal decouple of CO trends into 1990s, 2000s and 2010s. Representation of
560 non-uniform decrease in all decades mostly in SH whereas a continuous decrease in NH. But
561 a positive inter-decadal trend difference (δ-trend) reveals the weakening of decreasing trends
562 of CO in 2010s w.r.t to previous decades.

When it comes to 2010s, it is observed that trends are positive for 20 out of 49 stations. In fact, all 16 sites in SH (> 10 ^{o}S) have shown positive trends such that 15 sites had negative trends in 2000s. Though NH sites have continued to show negative trend in 2010s decade but a decline in the strength of decreasing trend has been observed for many NH sites, too. The inter-decadal trend difference (δ-trend) of 2010s and 2000s for each station showed positive δ-trend difference in total 41 out of 49 stations averaging to 0.96 ± 0.42 i.e. there is observed slowdown in decreasing rate of CO trends in 2010s (Figure 7). This *global reversal* of CO trends in 2010s is visible in many stations barring a few stations in Europe, Pacific and Atlantic. Figure 8 shows the sites where relative decadal changes i.e. relative uptrend/downtrend reversal during 2010s w.r.t. 2000s is observed. Sites of relative +ve δ-trend are observed in 41 out of 49 which means the strength of CO negative trends has been weakened at these sites in the recent decade of 2010s. Relative downtrend are the -ve δ-trend sites where CO is decreasing at a higher rate in 2010s than 2000s (Figure S7). It can be concluded that though the trends are still negative but CO is decreasing at a slower rate during 2010s with respect to 2000s. This conclusion is largely in consistent with (Buchholz et al., 2021) in which a global slowdown in the CO decline has been shown in 2010s as compared to CO trends from earlier studies using TIR CO satellite records from MOPITT, AIRS, TES, IASI. The reversal in CO trends in 2010s can have several reasons depending on the station location.

However, the large heterogeneity in the rate of decrease in each of the cluster (Table S1) points to strong local effects in addition to an overwhelming global effect like ENSO events pointing to increased CO emissions from a warming climate (Figures S3 and S2). The local effects can be either be change in emission patterns or the change in CO loss chemistry

588 mediated by the OH mixing ratios and recycling probabilities. Despite an overall global effort
589 in curbing emissions, the enhanced CO columns could be influenced by fire and
590 anthropogenic emissions (Buchholz et al., 2021). The overall decrease in CO coincides with
591 advancements in the combustion efficiency of anthropogenic sources (B Zheng et al., 2018),
592 a reduction in global fire emissions from 1997 to 2009 (van der Werf et al., 2010), and a
593 negative trend in burned area (Andela et al., 2017). Since 33% of the world's CO emissions
594 come from fire emission (Y. Yin et al., 2015), a trend in fires can have a significant impact
595 on atmospheric CO. (Buchholz et al., 2021; McDonald et al., 2013) suggests that the
596 slowdown in decreasing CO may be caused by diminishing returns from advancements in
597 combustion efficiency and emission controls. . This is because unlike NOx which have
598 predominant contributions from anthropogenic emissions, CO sources have competing
599 anthropogenic and natural/biomass burning components (Strode and Pawson, 2013).Thus CO
600 reduction efforts must consider fire mitigation and containment strategies. Despite opposite
601 trends in NOx over Korean (tap) and Japanese (mnm) sites (Figure S8 & Figure S10), the
602 decreasing effect on CO is more homogeneous (Figure S8). Apart from the atmospheric
603 chemistry component, the much longer lifetime of CO compared to NOx allows for
604 atmospheric transport mechanism to impact the CO budget. As transport patterns change
605 season wise, the seasonal variation of CO trends is investigated to understand the role of
606 atmospheric transport on CO trends.

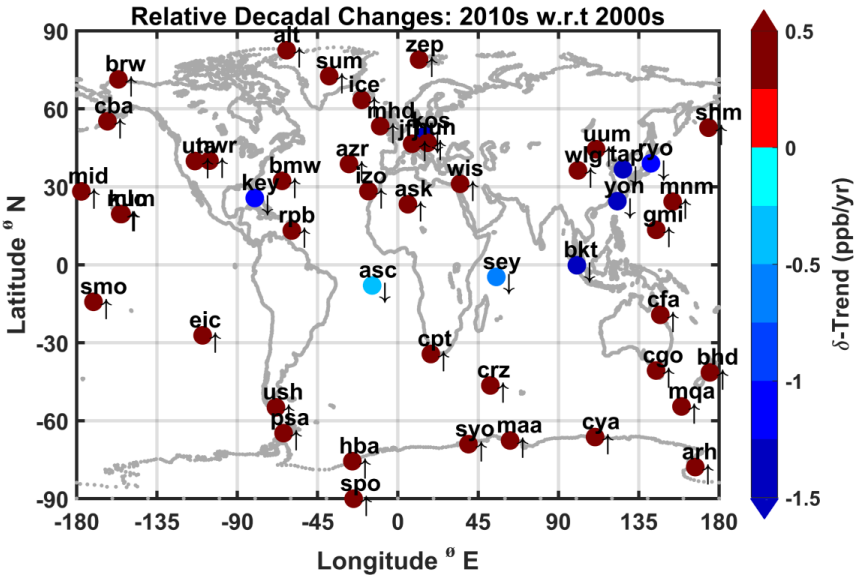

607

608 **Figure 8.** Spatial representation of relative decadal changes in growth rate in 2011-2020
609 decade with respect to 2001-2010. δ-Trend is the difference of growth rates in 2010s and
610 2000s. +ve difference in δ-Trend meaning the magnitude of negative growth rates in CO has
611 been reduced or have become positive and vice versa in the recent decade. Red/brown
612 markers are the spatially distributed 39 out of 49 sites depicting CO is decreasing with slower
613 rate or have positively increasing trend during 2010s with respect to 2000s.

614

615 **3.3.Seasonal variations in CO trends**

616 Peaks of CO mixing ratio are found from late winters to early springs and minimum during
617 summer season. In NH, February- March are the peak and July-August are the minimum CO
618 months (Figure 9, Table S2). Similarly, in SH, spring months i.e., September-October
619 exhibits the peak mixing ratios consistent with (Osman et al., 2016) . Biomass burning is very
620 favorable during this period on the south of equator due to which SH has sharper peaks than
621 NH (Chandra et al., 2016; Worden et al., 2013). A seasonal pattern in the inter-hemispheric
622 CO mixing ratio difference is observed with maximum difference 103-107 ppb) during
623 February-March (103-107 ppb) and a minimum difference (~34-35 ppb) (Figure 9) during
624 July-August. CO destruction by OH is high during summer (Khalil and Rasmussen, 1990).

Photolysis in the presence of higher temperature and atmospheric moisture results in high OH primary production in summer (Hildebrandt et al., 2010) leading to CO chemical losses by OH mediated oxidation resulting in reduced CO mixing ratios (Worden et al., 2013). Oxidation by OH also reduces the lifetime of CO to few weeks (~10 days) in summer whereas during winters its lifetime can extend to a few months (>60 days) (Holloway et al., 2000).

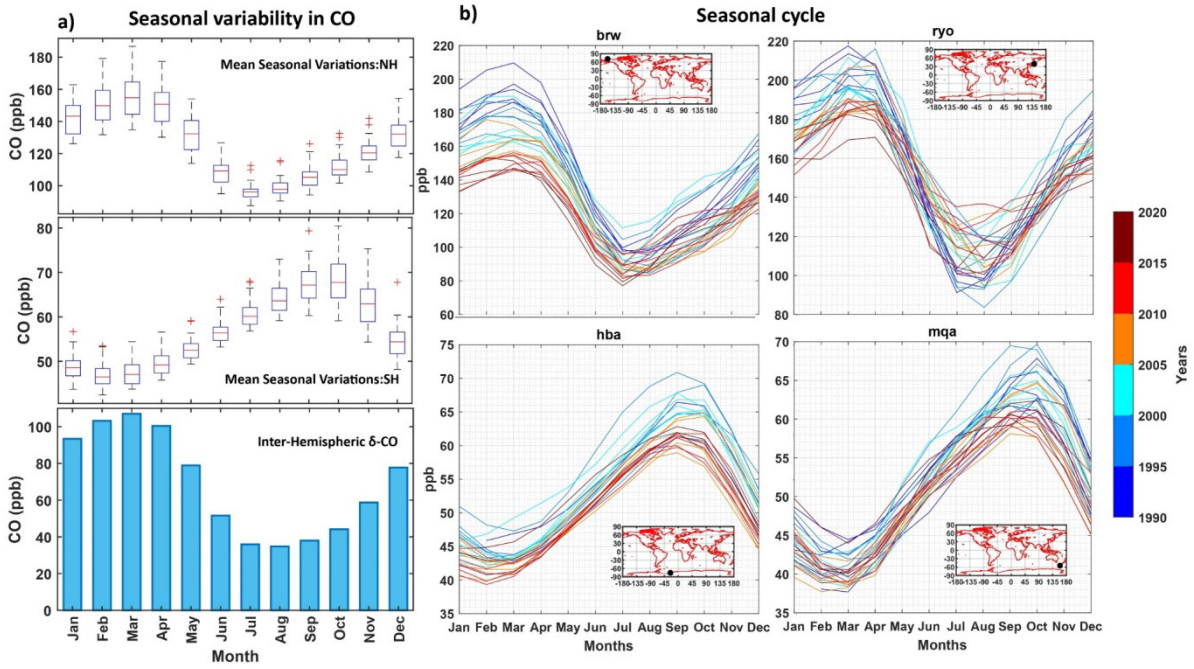

Figure 9. a) The box plot shows the average range of CO values varied in each month between 1991-2020. The variability of CO (ppb) values shows that highest differences are observed during Feb-March and lowest in July-August in between both hemispheres. b) Mean seasonal variations in CO Seasonal cycles of CO at 2 sites each in the NH (top row) and SH (bottom row). A blue to red color shift correspond to the reduction in the range of CO (ppb) seasonal.

Decomposition of the CO time series into seasonal trend component (1991-2020) reveals the season which has a dominant impact on CO trends. The seasonal trend analysis is performed for each meteorological season (Table S3) in NH and SH. Seasonal trend slopes are

calculated using the Sen Slope method on annually averaged season-wise CO values. In NH, decreasing trend is dominating in DJF and MAM seasons while in SH the overall trends are controlled by SON. There is a large difference (> -1.01 ppb/yr, $p<0.05$) in the inter-seasonal trends (between DJF, MAM and JJA, SON) at higher latitudes (50°N - 90°N) (Figure 10) i.e., CO is decreasing at a higher rate in winter and spring than other seasons at higher latitudes. Seasonal trends during DJF and MAM are close to ~ -1.35 to -1.48 ppb/yr, $p < 0.01$ for each respective station at this latitude belt and for JJA and SON are ~ -0.47 & -0.34 ppb/yr, $p < 0.01$. This dominancy of DJF and MAM is noticeable in NH and as going down south of equator SON starts dominating the decreasing trend, though magnitude of decreasing trends remains very low and barely falls below -0.5 ppb/yr in any season.

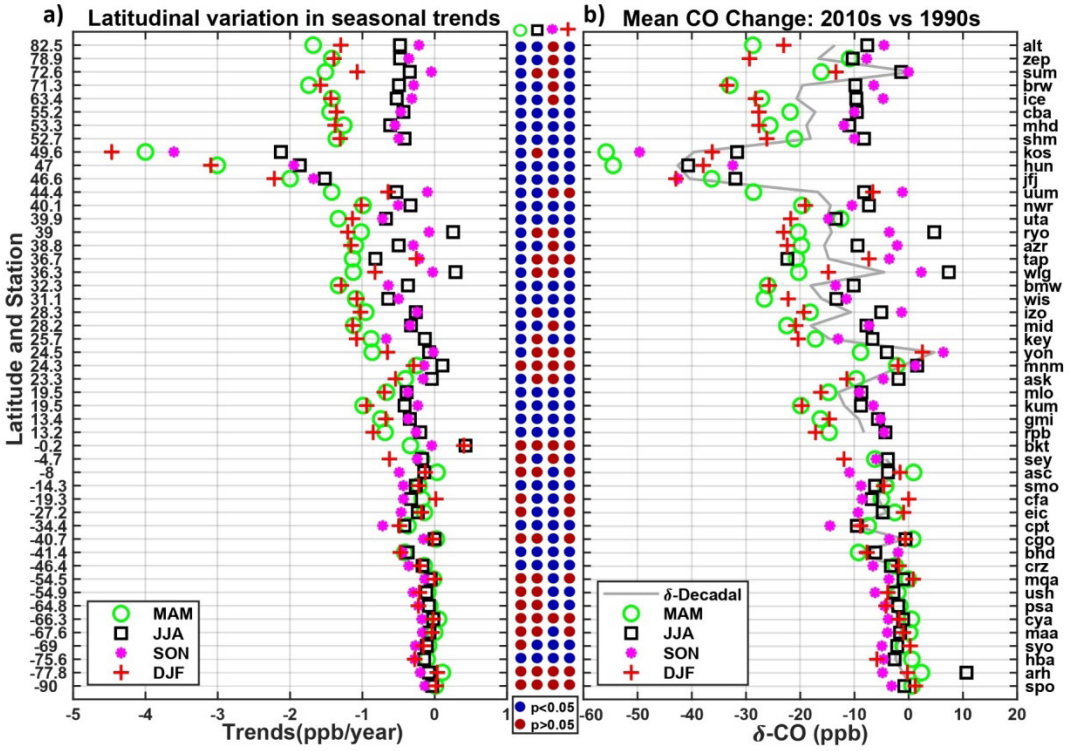

Figure 10. Latitudinal gradient of CO seasonal (DJF, MAM, JJA, SON) trends and overall decrease in CO mixing ratio during 1991-2020. Extreme negative trends in 40 °N -50 °N resulted in maximum CO (ppb) decrease over these sites (> -30 ppb) in all seasons. SON season dominated an average reduction of ~ 3.5 – 3.7 ppb in SH.

A difference of averaged decadal CO mixing ratio of 2010s and 1990s shows that on average, there is a decrease of -12.6 to -14.8 ppb, $p < 0.05$ in NH sites with large decreases (> -40 ppb) seenin 45ºN -50ºN (Figure 10). 50% of this is attributed to the JJA season, in which average decrease is -7.08 to -8.03 ppb, $p < 0.05$ in NH, while average decrease during the DJF and MAM seasons are -19.93 and -20.85 ppb, $p < 0.05$ respectively. Similarly, SH station also has shown average -3.5, $p < 0.05$ decreases over the period with the maximum decrease of -6.1 ppb, $p < 0.05$ during SON season and -3.7 ppb, $p < 0.05$ in other seasons. In NH, negative trends are observed consistent throughout the year. In contrast, SH exhibits most negative trends ($p<0.05$) specifically in SON season aligning with the most pronounced decline in CO levels occurs during the fire season along with global decrease in burned area reported by (Andela et al., 2017). Notably, the SON season has the most stations showing negative trends compared to other seasons (see Figure 10). This suggests that in other SH seasons, CO sources and sinks might be equilibrium, indicating that CO levels remain stable during these periods. In summary, in the NH, various factors contribute to the trend, including improved combustion efficiency, while in the SH, the main driver of CO level changes is wildfires (Buchholz et al., 2021).

While NH seasonal trends are dominated by negative values, 5 stations in South-East Asian region show positive trends during JJA (Figure 11). These stations are: ’bkt’ (Indonesia), ‘mnm’ (Japan), ‘ryo’ (Japan), ‘wlg’ (China), ‘yon’ (Japan). Atmospheric transport mechanisms are invoked to provide a first-hand explanation of these positive trends. During MAM season when CO mixing ratio is highest in the NH, it is seen that trends are less negative at `mnm' site in Pacific compared to mainland Korean and Japanese sites which are still much lower compared to mainland China sites. This gradual decrease in trends from mainland China to the east towards Japan and finally the ocean is supported by the wind

patterns. Coastal South China experiences a significant influence from subregional and regional-scale sources due to the multiscale transport and dispersion of air pollution. Influenced by the Asian monsoon, stations in South China are primarily affected by marine air from the South China Sea during the summer and by continental outflows from the Eurasian Continent. Consequently, the region serves as an excellent receptor for continental outflows, especially the regional emissions from East and South China (Ding et al., 2013; Wang et al., 2009; Zhang et al., 2011). (Ding et al., 2013) also concluded that the CO mixing ratios during JJA months are influenced by coastal regions in South China and East China, while North China is not a significant factor in this regard, considering the seasonal wind patterns and air mass trajectories.

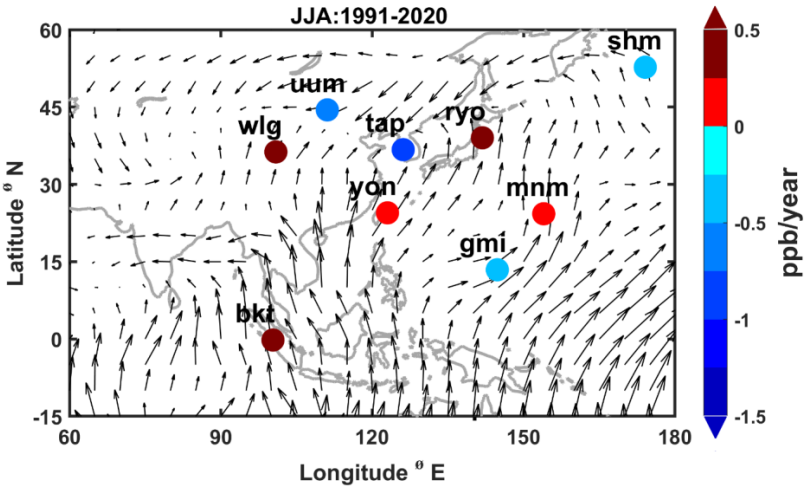

Figure 11. A contrasting positive trend over South-Asian sites during 1991-2020 in JJA season. 5 out of 9 sites had positive trends unlike other seasons.

It is to be noted that stations with positive trends (Figure 11) are non- significant ($p>0.05$) and there are several factors that leads to non-significance CO trends during summer season in this region. High variability in CO mixing ratios during these months can impact the significance of trends (Zhang et al., 2020). Also, major tropical fire hotspots (the islands of Kalimantan, Sumatra, and Papua; Indonesia) are in this region and fire emissions from these

boreal fires can be responsible for the weakening of the CO trend in this season (Buchholz et al., 2021; Fanin and van der Werf, 2017). This region has been affected by two strong biomass burning events in the middle of last two decades due to El-Nino events; one in 2006 and occurred from late 2014 to early 2016. These biomass burning events have also contributed to the increase in CO mole fractions (Babu et al., 2021; Fadnavis et al., 2019; Ribeiro et al., 2020). CO trends indicates negative trends in this region when 2015 El-Nino driven fires are excluded from the analysis(Jiang et al., 2017). Furthermore, agricultural burning, which typically peaks in June (Li et al., 2018; Wu et al., 2017), may potentially be a factor in the elevated CO levels. Studies have suggested an increase in strength of the summer monsoon rainfall over China and a decrease in number dry days (Li and Hu, 2019). A possible result of this may be the observed increase cloud cover (Cai et al., 2017) leading to decreased primary production of OH and hence decreased photochemical losses of CO causing an enhancement in trend.

(Xiong et al., 2022) provided long term seasonal analysis between 2004-2019 at higher altitude site in China ('wlg'). This study revealed that there was a distinct increasing trend for the amplitude of CO mole fraction in diurnal cycle in summer., The highest CO mole fractions increased from 152.3 ± 7.4 ppb in to 180.4 ± 20.3 ppb between 2004-2019 specifically to daytime in summer season. CO generally peaks in afternoon and then decreases in other seasons but it was observed that in summer it rises again from afternoon and reaches maximum value in dusk. In this season, the strengthening of wind (Wang et al., 2006) in the afternoon is responsible for local transport of emitted CO to 'wlg' which lead to second peak at dusk. In the nearby Chinese province of Qinghai, urban industrialization led to extensive fossil fuel consumption, which increased CO_2 emissions from 19.0 MT to 51.9 MT between 2004 and 2018, with coal accounting for most of that increase having highest

peak of 212.0 MT in 2014-2015. In Gansu (another nearby province) also CO_2 emission reached to highest peak of 209.0 MT in 2015. Due to the significant contribution of this, CO emissions in urban areas increased over time and eventually reached 'wlg' with air masses (Lin et al., 2011; Xiong et al., 2022)

MOPITT constrained inverse analysis suggested decreasing CO emissions from east China (Strode and Pawson, 2013; Worden et al., 2013) between 2008-2014 however there is an increase of 6 ppb in CO concentrations over the outflow of east China during this period (Jiang et al., 2017). This increase has been influenced by a considerable increase in anthropogenic emissions from India and southeast Asia and this could be a possible reason for the rise in CO concentration that WDCGG stations have reported in this region (Jiang et al., 2015).

4. Conclusions

This study utilizes the observations from 49 stations across the globe to understand the CO trend during 1991-2020. It mainly shows

1. Atmospheric CO exhibits a decreasing trend during 1991-2020 although it is not homogenously decreasing globally on spatial and temporal scale.
2. CO changes have a latitudinal and regional dependency. Negative trends are more prominent in northern higher latitudes. Sites in midlatitudes (23.5°N-66.5°N) have the highest CO mixing ratio (150-250 ppb) and most negative trends. Trend ranges from -0.35 to -3.77 ppb/year between 25°N -90°N and -0.02 to -0.46 ppb/year between 25°S -90°S. Different regions have different rates of decreasing trends within the

hemisphere i.e., European continent has higher decreasing trends than USA and Asian continent in NH. When it comes to emissions, there a difference on CO growth rate, depending on where CO emission change occurred. If CO emissions changed in the high latitudes (long lifetime region) the effect on CO growth rate is bigger, and any change in CO emission in the tropical latitudes (short lifetime region) has lesser impact on CO growth rate.

3. There is strong inter-hemispheric gradient in decreasing trend and in CO mixing ratio. The peak CO mixing ratio of every SH site are below the base mixing ratio of NH sites. A maximum difference in CO (ppb) between NH and SH is 103-107 ppb during Feb-Mar and minimum difference of 35-36 ppb during July-August.
4. CO was decreasing with stronger rate till 2000s but a reversal is observed in 2010s as the strength of decreasing CO has weakened in 2010-2020 decade. Given that the global total emissions did not increase much in 2001-2010, it may be related to several factors like ENSO modulating interdecadal CO growth rate highlighting the relevance of climate vis a vis emissions in modulating the growth rate.
5. Our analysis points to a weakening of the negative growth rate in CO in the 2011-2020 period compared to the previous decade. This observation, however, does not imply that the recent reduction in growth rate will continue to weaken in future or even turn in to an increasing trend. However, these observations provide a challenging background for modeling studies of CO to understand past trends under different scenarios of emission and project for the future possibilities. Both the emission and loss budget scenarios must be considered in order to explain the CO trends.
6. Among all regional clusters, Cluster-1 (European region) showed a largest and continuous decrease in CO in 1991-2020.

7. NH sites have maximum CO in DJF-MAM seasons and SON season dominates in SH.
8. There is an average reduction of -16.22 ± 1.92 ppb and -4.5 ± 0.64 ppb CO in the NH and SH respectively between 1991-2020.

Acknowledgements. This work is partly supported by the Environment Research and Technology Development Fund (JPMEERF20172001, JPMEERF20182002) of the Ministry of the Environment, Japan. AP sincerely acknowledges the financial support provided by DST INSPIRE Scholarship for higher studies. The modeled OH and NOx data simulated by JAMSTEC's MIROC-Chem were downloaded from https://tes.jpl.nasa.gov/tes/chemical-reanalysis/products/ (last accessed: on January 5, 2021). The CO datasets are downloaded from the World Data Centre for Greenhouse Gases (WDCGG) hosted by Japan Meteorological Agency (JMA). We appreciate the efforts by the WMO/WDCGG for preparing harmonized data from various national agencies. The authors also sincerely thank Paul Krummel and Ray Langenfelds from CSIRO for their comments which have improved quality of this manuscript. CSIRO is also one the data providers. MS acknowledges funding from the GAW Quality Assurance/Science Activity Centre Switzerland (QA/SAC-CH) which is supported by MeteoSwiss and Empa. CM thanks JAMSTEC and Dr Prabir Patra for the visiting position when this collaborative work was initiated. CM thanks ISRO-GBP:ATCTM project for funding support. We thank from the bottom of our heart the three anonymous reviewers for going thorugh this MS in minute details and providing their extensive comments which has improved this MS significantly. We sincerely thank the editor for getting this MS reviewed.

References:

Andela, N., Morton, D.C., Giglio, L., Chen, Y., Van Der Werf, G.R., Kasibhatla, P.S.,

DeFries, R.S., Collatz, G.J., Hantson, S., Kloster, S., Bachelet, D., Forrest, M., Lasslop, G., Li, F., Mangeon, S., Melton, J.R., Yue, C., Randerson, J.T., 2017. A human-driven decline in global burned area. Science (80-.). 356, 1356 – 1362. https://doi.org/10.1126/science.aal4108

Babu, S.R., Ratnam, M.V., Basha, G., Kumar Pani, S., Lin, N.-H., 2021. Structure, dynamics, and trace gas variability within the asian summer monsoon anticyclone in the extreme el niño of 2015-2016. Atmos. Chem. Phys. 21, 5533 – 5547. https://doi.org/10.5194/acp-21-5533-2021

Belikov, D.A., Saitoh, N., Patra, P.K., 2022. An Analysis of Interhemispheric Transport Pathways Based on Three-Dimensional Methane Data by GOSAT Observations and Model Simulations. J. Geophys. Res. Atmos. 127, e2021JD035688. https://doi.org/https://doi.org/10.1029/2021JD035688

Bowman, D.M.J.S., Kolden, C.A., Abatzoglou, J.T., Johnston, F.H., van der Werf, G.R., Flannigan, M., 2020. Vegetation fires in the Anthropocene. Nat. Rev. Earth Environ. 1, 500–515. https://doi.org/10.1038/s43017-020-0085-3

Bradley, K.S., Stedman, D.H., Bishop, G.A., 1999. A global inventory of carbon monoxide emissions from motor vehicles. Chemosph. - Glob. Chang. Sci. 1, 65–72. https://doi.org/10.1016/S1465-9972(99)00017-3

Buchholz, R.R., Worden, H.M., Park, M., Francis, G., Deeter, M.N., Edwards, D.P., Emmons, L.K., Gaubert, B., Gille, J., Martínez-Alonso, S., Tang, W., Kumar, R., Drummond, J.R., Clerbaux, C., George, M., Coheur, P.F., Hurtmans, D., Bowman, K.W., Luo, M., Payne, V.H., Worden, J.R., Chin, M., Levy, R.C., Warner, J., Wei, Z., Kulawik, S.S., 2021. Air pollution trends measured from Terra: CO and AOD over industrial, fire-prone, and background regions. Remote Sens. Environ. 256, 112275. https://doi.org/10.1016/j.rse.2020.112275

827 Cai, H., Feng, X., Chen, Q., Sun, Y., Wu, Z., Tie, X., 2017. Spatial and Temporal Features of
828 the Frequency of Cloud Occurrence over China Based on CALIOP. Adv. Meteorol.
829 2017. https://doi.org/10.1155/2017/4548357
830 Canadell, J.G., Meyer, C.P. (Mick), Cook, G.D., Dowdy, A., Briggs, P.R., Knauer, J., Pepler,
831 A., Haverd, V., 2021. Multi-decadal increase of forest burned area in Australia is linked
832 to climate change. Nat. Commun. 12, 6921. https://doi.org/10.1038/s41467-021-27225-4
833 Chandra, N., Patra, P.K., Niwa, Y., Ito, A., Iida, Y., Goto, D., Morimoto, S., Kondo, M.,
834 Takigawa, M., Hajima, T., Watanabe, M., 2022. Estimated regional CO2 flux and
835 uncertainty based on an ensemble of atmospheric CO2 inversions. Atmos. Chem. Phys.
836 22, 9215–9243. https://doi.org/10.5194/acp-22-9215-2022
837 Chandra, N., Venkataramani, S., Lal, S., Sheel, V., Pozzer, A., 2016. Effects of convection
838 and long-range transport on the distribution of carbon monoxide in the troposphere over
839 India. Atmos. Pollut. Res. 7, 775–785. https://doi.org/10.1016/j.apr.2016.03.005
840 Chen, Y., Hall, J., van Wees, D., Andela, N., Hantson, S., Giglio, L., van der Werf, G.R.,
841 Morton, D.C., Randerson, J.T., 2023. Multi-decadal trends and variability in burned area
842 from the 5th version of the Global Fire Emissions Database (GFED5). Earth Syst. Sci.
843 Data Discuss. 2023, 1–52. https://doi.org/10.5194/essd-2023-182
844 Crippa, M., Gabriel, O., Diego, G., Marilena, M., Edwin, S., Eleonora, L.V., Efisio, S., Fabio,
845 M.-F., Jos, O., 2019. Fossil CO2 and GHG emissions of all world countries. J. Geophys.
846 Res. Atmos. 105, 1867–1877.
847 Crippa, M., Guizzardi, D., Butler, T., Keating, T., Wu, R., Kaminski, J., Kuenen, J.,
848 Kurokawa, J., Chatani, S., Morikawa, T., Pouliot, G., Racine, J., Moran, M.D., Klimont,
849 Z., Manseau, P.M., Mashayekhi, R., Henderson, B.H., Smith, S.J., Suchyta, H., Muntean,
850 M., Solazzo, E., Banja, M., Schaaf, E., Pagani, F., Woo, J.-H., Kim, J., Monforti-
851 Ferrario, F., Pisoni, E., Zhang, J., Niemi, D., Sassi, M., Ansari, T., Foley, K., 2023. The

852 HTAP_v3 emission mosaic: merging regional and global monthly emissions (2000--
853 2018) to support air quality modelling and policies. Earth Syst. Sci. Data 15, 2667–2694.
854 https://doi.org/10.5194/essd-15-2667-2023
855 Crippa, M., Janssens-Maenhout, G., Dentener, F., Guizzardi, D., Sindelarova, K., Muntean,
856 M., Van Dingenen, R., Granier, C., 2016. Forty years of improvements in European air
857 quality: Regional policy-industry interactions with global impacts. Atmos. Chem. Phys.
858 16, 3825–3841. https://doi.org/10.5194/acp-16-3825-2016
859 Crotwell, A., Lee, H., Steinbacher, M., 2018. 19th WMO/IAEA Meeting on Carbon Dioxide,
860 Other Greenhouse Gases and Related Measurement Techniques (GGMT-2017). Glob.
861 Atmos. Watch Rep. 1–141.
862 Deeter, M.N., Edwards, D.P., Gille, J.C., Worden, H.M., 2015. Information content of
863 MOPITT CO profile retrievals: Temporal and geographical variability. J. Geophys. Res.
864 120, 12,723-12,738. https://doi.org/10.1002/2015JD024024
865 Ding, A., Wang, T., Fu, C., 2013. Transport characteristics and origins of carbon monoxide
866 and ozone in Hong Kong, South China. J. Geophys. Res. Atmos. 118, 9475–9488.
867 https://doi.org/10.1002/jgrd.50714
868 Ehhalt, D., Prather, M., 2001. Atmospheric Chemistry and Greenhouse Gases. Clim. Chang.
869 2001 Sci. Basis 239–287.
870 Fadnavis, S., Sabin, T.P., Roy, C., Rowlinson, M., Rap, A., Vernier, J.-P., Sioris, C.E., 2019.
871 Elevated aerosol layer over South Asia worsens the Indian droughts. Sci. Rep. 9.
872 https://doi.org/10.1038/s41598-019-46704-9
873 Fan, H., Yang, X., Zhao, C., Yang, Y., Shen, Z., 2023. Spatiotemporal variation
874 characteristics of global fires and their emissions. Atmos. Chem. Phys. 23, 7781–7798.
875 https://doi.org/10.5194/acp-23-7781-2023
876 Fanin, T., van der Werf, G.R., 2017. Precipitation--fire linkages in Indonesia (1997--2015).

877 Biogeosciences 14, 3995–4008. https://doi.org/10.5194/bg-14-3995-2017
878 Frederiksen, J.S., Francey, R.J., 2018. Unprecedented strength of Hadley circulation in 2015–
879 2016 impacts on CO2 interhemispheric difference. Atmos. Chem. Phys. 18, 14837–
880 14850. https://doi.org/10.5194/acp-18-14837-2018
881 Gaubert, B., Arellano Jr., A.F., Barré, J., Worden, H.M., Emmons, L.K., Tilmes, S.,
882 Buchholz, R.R., Vitt, F., Raeder, K., Collins, N., Anderson, J.L., Wiedinmyer, C.,
883 Martinez Alonso, S., Edwards, D.P., Andreae, M.O., Hannigan, J.W., Petri, C., Strong,
884 K., Jones, N., 2016. Toward a chemical reanalysis in a coupled chemistry-climate
885 model: An evaluation of MOPITT CO assimilation and its impact on tropospheric
886 composition. J. Geophys. Res. Atmos. 121, 7310–7343.
887 https://doi.org/https://doi.org/10.1002/2016JD024863
888 Gaubert, B., Worden, H.M., Arellano, A.F.J., Emmons, L.K., Tilmes, S., Barré, J., Martinez
889 Alonso, S., Vitt, F., Anderson, J.L., Alkemade, F., Houweling, S., Edwards, D.P., 2017.
890 Chemical Feedback From Decreasing Carbon Monoxide Emissions. Geophys. Res. Lett.
891 44, 9985–9995. https://doi.org/10.1002/2017GL074987
892 Gerbig, C., Schmitgen, S., Kley, D., Volz-Thomas, A., Dewey, K., Haaks, D., 1999. An
893 improved fast-response vacuum-UV resonance fluorescence CO instrument. J. Geophys.
894 Res. Atmos. 104, 1699–1704. https://doi.org/https://doi.org/10.1029/1998JD100031
895 Guan, Y., Shan, Y., Huang, Q., Chen, H., Wang, D., Hubacek, K., 2021. Assessment to
896 China's Recent Emission Pattern Shifts. Earth's Futur. 9, e2021EF002241.
897 https://doi.org/https://doi.org/10.1029/2021EF002241
898 Hallock-Waters, K.A., Doddridge, B.G., Dickerson, R.R., Spitzer, S., Ray, J.D., 1999.
899 Carbon monoxide in the U.S. Mid-Atlantic troposphere: Evidence for a decreasing trend.
900 Geophys. Res. Lett. 26, 2861–2864. https://doi.org/10.1029/1999GL900609
901 Hedelius, J.K., Toon, G.C., Buchholz, R.R., Iraci, L.T., Podolske, J.R., Roehl, C.M.,

902 Wennberg, P.O., Worden, H.M., Wunch, D., 2021. Regional and Urban Column CO
903 Trends and Anomalies as Observed by MOPITT Over 16 Years. J. Geophys. Res.
904 Atmos. 126, 1–18. https://doi.org/10.1029/2020JD033967
905 Hildebrandt, L., Kostenidou, E., Mihalopoulos, N., Worsnop, D.R., Donahue, N.M., Pandis,
906 S.N., 2010. Formation of highly oxygenated organic aerosol in the atmosphere: Insights
907 from the Finokalia Aerosol Measurement Experiments. Geophys. Res. Lett. 37, 6–10.
908 https://doi.org/10.1029/2010GL045193
909 Holloway, T., Levy, H., Kasibhatla, P., 2000. Global distribution of carbon monoxide. J.
910 Geophys. Res. Atmos. 105, 12123–12147. https://doi.org/10.1029/1999JD901173
911 Hung, H., Blanchard, P., Halsall, C.J., Bidleman, T.F., Stern, G.A., Fellin, P., Muir, D.C.G.,
912 Barrie, L.A., Jantunen, L.M., Helm, P.A., Ma, J., Konoplev, A., 2005. Temporal and
913 spatial variabilities of atmospheric polychlorinated biphenyls (PCBs), organochlorine
914 (OC) pesticides and polycyclic aromatic hydrocarbons (PAHs) in the Canadian Arctic:
915 Results from a decade of monitoring. Sci. Total Environ. 342, 119–144.
916 https://doi.org/10.1016/j.scitotenv.2004.12.058
917 Jiang, Y., Zhou, L., Raghavendra, A., 2020. Observed changes in fire patterns and possible
918 drivers over Central Africa. Environ. Res. Lett. 15, 2000–2010.
919 https://doi.org/10.1088/1748-9326/ab9db2
920 Jiang, Z., Worden, J.R., Jones, D.B.A., Lin, J.-T., Verstraeten, W.W., Henze, D.K., 2015.
921 Constraints on Asian ozone using Aura TES, OMI and Terra MOPITT. Atmos. Chem.
922 Phys. 15, 99–112. https://doi.org/10.5194/acp-15-99-2015
923 Jiang, Z., Worden, J.R., Worden, H., Deeter, M., Jones, D.B.A., Arellano, A.F., Henze, D.K.,
924 2017. A fifteen year record of CO emissions constrained by MOPITT CO observations.
925 Atmos. Chem. Phys. Discuss. 1–46. https://doi.org/10.5194/acp-2016-811
926 Jindal, P., Thapliyal, P.K., Shukla, M.V., Sharma, S.K., Mitra, D., 2020. Trend analysis of

927 atmospheric temperature, water vapour, ozone, methane and carbon-monoxide over few
928 major cities of India using satellite data. J. Earth Syst. Sci. 129.
929 https://doi.org/10.1007/s12040-019-1325-0
930 Kamal, N., Pachauri, S., 2019. Mann-Kendall, and Sen's Slope Estimators for Precipitation
931 Trend Analysis in North-Eastern States of India. Int. J. Comput. Appl. 177, 7–16.
932 https://doi.org/10.5120/ijca2019919453
933 Khalil, M.A.K., Rasmussen, R.A., 1990. Atmospheric carbon monoxide: Latitudinal
934 distribution of sources. Geophys. Res. Lett. 17, 1913–1916.
935 https://doi.org/10.1029/GL017i011p01913
936 Kuklinska, K., Wolska, L., Namiesnik, J., 2015. Air quality policy in the U.S. and the EU – a
937 review. Atmos. Pollut. Res. 6, 129–137.
938 https://doi.org/https://doi.org/10.5094/APR.2015.015
939 Kurokawa, J., Ohara, T., Morikawa, T., Hanayama, S., Janssens-Maenhout, G., Fukui, T.,
940 Kawashima, K., Akimoto, H., 2013. Emissions of air pollutants and greenhouse gases
941 over Asian regions during 2000–2008: Regional Emission inventory in ASia (REAS)
942 version 2. Atmos. Chem. Phys. 13, 11019–11058. https://doi.org/10.5194/acp-13-11019-
943 2013
944 Lelieveld, J., Dentener, F.J., Peters, W., Krol, M.C., 2004. On the role of hydroxyl radicals in
945 the self-cleansing capacity of the troposphere. Atmos. Chem. Phys. 4, 2337–2344.
946 https://doi.org/10.5194/acp-4-2337-2004
947 Lelieveld, J., Gromov, S., Pozzer, A., Taraborrelli, D., 2016. Global tropospheric hydroxyl
948 distribution, budget and reactivity. Atmos. Chem. Phys. 16, 12477–12493.
949 https://doi.org/10.5194/acp-16-12477-2016
950 Li, Meng, Liu, H., Geng, G., Hong, C., Liu, F., Song, Y., Tong, D., Zheng, B., Cui, H., Man,
951 H., Zhang, Q., He, K., 2017. Anthropogenic emission inventories in China: a review.

952 Natl. Sci. Rev. 4, 834–866. https://doi.org/10.1093/nsr/nwx150
953 Li, M., Wang, T., Xie, M., Li, S., Zhuang, B., Chen, P., Huang, X., Han, Y., 2018.
954 Agricultural Fire Impacts on Ozone Photochemistry Over the Yangtze River Delta
955 Region, East China. J. Geophys. Res. Atmos. 123, 6605–6623.
956 https://doi.org/https://doi.org/10.1029/2018JD028582
957 Li, M, Zhang, Q., Kurokawa, J.-I., Woo, J.-H., He, K., Lu, Z., Ohara, T., Song, Y., Streets,
958 D.G., Carmichael, G.R., Cheng, Y., Hong, C., Huo, H., Jiang, X., Kang, S., Liu, F., Su,
959 H., Zheng, B., 2017. MIX: a mosaic Asian anthropogenic emission inventory under the
960 international collaboration framework of the MICS-Asia and HTAP. Atmos. Chem.
961 Phys. 17, 935–963. https://doi.org/10.5194/acp-17-935-2017
962 Li, X., Hu, Q., 2019. Spatiotemporal Changes in Extreme Precipitation and Its Dependence
963 on Topography over the Poyang Lake Basin, China. Adv. Meteorol. 2019.
964 https://doi.org/10.1155/2019/1253932
965 Li, Y., Ma, Z., Han, T., Quan, W., Wang, J., Zhou, H., He, D., Dong, F., 2022. Long-term
966 declining in carbon monoxide (CO) at a rural site of Beijing during 2006–2018 implies
967 the improved combustion efficiency and effective emission control. J. Environ. Sci.
968 (China) 115, 432–442. https://doi.org/10.1016/j.jes.2020.11.011
969 Lin, Y.C., Lin, C.Y., Lin, P.H., Engling, G., Lan, Y.-Y., Kuo, T.-H., Hsu, W.T., Ting, C.-C.,
970 2011. Observations of ozone and carbon monoxide at Mei-Feng mountain site
971 (2269ma.s.l.) in Central Taiwan: Seasonal variations and influence of Asian continental
972 outflow. Sci. Total Environ. 409, 3033–3042.
973 https://doi.org/https://doi.org/10.1016/j.scitotenv.2011.04.023
974 M, C., D, G., M, M., E, S., 2021. EDGAR v5.0 Global Air Pollutant Emissions.
975 Mallik, C., Tomsche, L., Bourtsoukidis, E., Crowley, J.N., Derstroff, B., Fischer, H.,
976 Hafermann, S., Hüser, I., Javed, U., Keßel, S., Lelieveld, J., Martinez, M., Meusel, H.,

977 Novelli, A., Phillips, G.J., Pozzer, A., Reiffs, A., Sander, R., Taraborrelli, D., Sauvage,
978 C., Schuladen, J., Su, H., Williams, J., Harder, H., 2018. Oxidation processes in the
979 eastern Mediterranean atmosphere: Evidence from the modelling of HOx measurements
980 over Cyprus. Atmos. Chem. Phys. 18, 10825–10847. https://doi.org/10.5194/acp-18-
981 10825-2018
982 McDonald, B.C., Gentner, D.R., Goldstein, A.H., Harley, R.A., 2013. Long-Term Trends in
983 Motor Vehicle Emissions in U.S. Urban Areas. Environ. Sci. \& Technol. 47, 10022–
984 10031. https://doi.org/10.1021/es401034z
985 Miyazaki, K., Bowman, K., Sekiya, T., Eskes, H., Boersma, F., Worden, H., Livesey, N.,
986 Payne, V.H., Sudo, K., Kanaya, Y., Takigawa, M., Ogochi, K., 2020. Updated
987 tropospheric chemistry reanalysis and emission estimates, TCR-2, for 2005–2018. Earth
988 Syst. Sci. Data 12, 2223–2259. https://doi.org/10.5194/essd-12-2223-2020
989 Miyazaki, K., Eskes, H., Sudo, K., Boersma, K.F., Bowman, K., Kanaya, Y., 2017. Decadal
990 changes in global surface NOx emissions from multi-constituent satellite data
991 assimilation. Atmos. Chem. Phys. 17, 807–837. https://doi.org/10.5194/acp-17-807-
992 2017
993 Myhre, G., Samset, B.H., Schulz, M., Balkanski, Y., Bauer, S., Berntsen, T.K., Bian, H.,
994 Bellouin, N., Chin, M., Diehl, T., Easter, R.C., Feichter, J., Ghan, S.J., Hauglustaine, D.,
995 Iversen, T., Kinne, S., Kirkeväg, A., Lamarque, J.F., Lin, G., Liu, X., Lund, M.T., Luo,
996 G., Ma, X., Van Noije, T., Penner, J.E., Rasch, P.J., Ruiz, A., Seland, Skeie, R.B., Stier,
997 P., Takemura, T., Tsigaridis, K., Wang, P., Wang, Z., Xu, L., Yu, H., Yu, F., Yoon, J.H.,
998 Zhang, K., Zhang, H., Zhou, C., 2013. Radiative forcing of the direct aerosol effect from
999 AeroCom Phase II simulations. Atmos. Chem. Phys. 13, 1853–1877.
1000 https://doi.org/10.5194/acp-13-1853-2013
1001 Nakazawa, T., Ishizawa, M., Higuchi, K., Trivett, N.B.A., 1997a. TWO CURVE FITTING

1002 METHODS APPLIED TO CO2 FLASK DATA. Environmetrics 8, 197–218.
1003 Nakazawa, T., Ishizawa, M., Higuchi, K., Trivett, N.B.A., 1997b. Two curve fitting methods
1004 applied to CO2 flask data. Environmetrics 8, 197–218.
1005 https://doi.org/10.1002/(SICI)1099-095X(199705)8:3<197::AID-ENV248>3.0.CO;2-C
1006 Nguyen, N.H., Turner, A.J., Yin, Y., Prather, M.J., Frankenberg, C., 2020. Effects of
1007 Chemical Feedbacks on Decadal Methane Emissions Estimates. Geophys. Res. Lett. 47.
1008 https://doi.org/10.1029/2019GL085706
1009 NOAA, 2020. Multivariate ENSO Index Version 2 (MEI. v2).
1010 NOAA, 2018. Carbon Monoxide (CO) WMO Scale [WWW Document]. URL
1011 https://gml.noaa.gov/ccl/co_scale.html
1012 Novelli, P.C., Masarie, K.A., Lang, P.M., 1998. Distributions and recent changes of carbon
1013 monoxide in the lower troposphere. J. Geophys. Res. Atmos. 103, 19015–19033.
1014 https://doi.org/10.1029/98JD01366
1015 Novelli, P.C., Masarie, K.A., Lang, P.M., Hall, B.D., Myers, R.C., Elkins, J.W., 2003.
1016 Reanalysis of tropospheric CO trends: Effects of the 1997-1998 wildfires. J. Geophys.
1017 Res. Atmos. 108. https://doi.org/10.1029/2002jd003031
1018 Ohneiser, K., Ansmann, A., Kaifler, B., Chudnovsky, A., Barja, B., Knopf, D.A., Kaifler, N.,
1019 Baars, H., Seifert, P., Villanueva, D., Jimenez, C., Radenz, M., Engelmann, R.,
1020 Veselovskii, I., Zamorano, F., 2022. Australian wildfire smoke in the stratosphere: the
1021 decay phase in 2020/2021 and impact on ozone depletion. Atmos. Chem. Phys. 22,
1022 7417–7442. https://doi.org/10.5194/acp-22-7417-2022
1023 Oreggioni, G.D., Mahiques, O., Monforti-Ferrario, F., Schaaf, E., Muntean, M., Guizzardi, D.,
1024 Vignati, E., Crippa, M., 2022. The impacts of technological changes and regulatory
1025 frameworks on global air pollutant emissions from the energy industry and road
1026 transport. Energy Policy 168, 113021.

https://doi.org/https://doi.org/10.1016/j.enpol.2022.113021

Osman, M.K., Tarasick, D.W., Liu, J., Moeini, O., Thouret, V., Fioletov, V.E., Parrington, M., Nédélec, P., 2016. Carbon monoxide climatology derived from the trajectory mapping of global MOZAIC-IAGOS data. Atmos. Chem. Phys. 16, 10263–10282. https://doi.org/10.5194/acp-16-10263-2016

Patra, P.K., Krol, M.C., Montzka, S.A., Arnold, T., Atlas, E.L., Lintner, B.R., Stephens, B.B., Xiang, B., Elkins, J.W., Fraser, P.J., Ghosh, A., Hintsa, E.J., Hurst, D.F., Ishijima, K., Krummel, P.B., Miller, B.R., Miyazaki, K., Moore, F.L., Mühle, J., O'Doherty, S., Prinn, R.G., Steele, L.P., Takigawa, M., Wang, H.J., Weiss, R.F., Wofsy, S.C., Young, D., 2014. Observational evidence for interhemispheric hydroxyl-radical parity. Nature 513, 219–223. https://doi.org/10.1038/nature13721

Patra, P.K., Krol, M.C., Prinn, R.G., Takigawa, M., Mühle, J., Montzka, S.A., Lal, S., Yamashita, Y., Naus, S., Chandra, N., Weiss, R.F., Krummel, P.B., Fraser, P.J., O'Doherty, S., Elkins, J.W., 2021. Methyl Chloroform Continues to Constrain the Hydroxyl (OH) Variability in the Troposphere. J. Geophys. Res. Atmos. 126. https://doi.org/10.1029/2020JD033862

Patra, P.K., Maksyutov, S., Nakazawa, T., 2005. Analysis of atmospheric CO_2 growth rates at Mauna Loa using CO_2 fluxes derived from an inverse model. Tellus B Chem. Phys. Meteorol. 57, 357. https://doi.org/10.3402/tellusb.v57i5.16560

Pickers, P.A., Manning, A.C., 2015. Investigating bias in the application of curve fitting programs to atmospheric time series. Atmos. Meas. Tech. 8, 1469–1489. https://doi.org/10.5194/amt-8-1469-2015

Ribeiro, I.O., do Santos, E.O., Batista, C.E., Fernandes, K.S., Ye, J., Medeiros, A.S., e Oliveira, R.L., de Sá, S.S., de Sousa, T.R., Kayano, M.T., Andreoli, R. V., Machado, C. de M.D., Surratt, J.D., Junior, S.D., Martin, S.T., de Souza, R.A.F., 2020. Impact of

biomass burning on a metropolitan area in the Amazon during the 2015 El Niño: The enhancement of carbon monoxide and levoglucosan concentrations. Environ. Pollut. 260. https://doi.org/10.1016/j.envpol.2020.114029

Rosanka, S., Frömming, C., Grewe, V., 2020. The impact of weather patterns and related transport processes on aviation's contribution to ozone and methane concentrations from \chem{NO_\mathit{x}} emissions. Atmos. Chem. Phys. 20, 12347–12361. https://doi.org/10.5194/acp-20-12347-2020

Safieddine, S.A., Heald, C.L., Henderson, B.H., 2017. The global nonmethane reactive organic carbon budget: A modeling perspective. Geophys. Res. Lett. 44, 3897–3906. https://doi.org/10.1002/2017GL072602

Shindell, D.T., Faluvegi, G., Stevenson, D.S., Krol, M.C., Emmons, L.K., Lamarque, J.F., Pétron, G., Dentener, F.J., Ellingsen, K., Schultz, M.G., Wild, O., Amann, M., Atherton, C.S., Bergmann, D.J., Bey, I., Butler, T., Cofala, J., Collins, W.J., Derwent, R.G., Doherty, R.M., Drevet, J., Eskes, H.J., Fiore, A.M., Gauss, M., Hauglustaine, D.A., Horowitz, L.W., Isaksen, I.S.A., Lawrence, M.G., Montanaro, V., Müller, J.F., Pitari, G., Prather, M.J., Pyle, J.A., Rast, S., Rodriguz, J.M., Sanderson, M.G., Savage, N.H., Strahan, S.E., Sudo, K., Szopa, S., Unger, N., van Noije, T.P.C., Zeng, G., 2006. Multimodel simulations of carbon monoxide: Comparison with observations and projected near-future changes. J. Geophys. Res. Atmos. 111. https://doi.org/10.1029/2006JD007100

Strode, S.A., Duncan, B.N., Yegorova, E.A., Kouatchou, J., Ziemke, J.R., Douglass, A.R., 2015. Implications of carbon monoxide bias for methane lifetime and atmospheric composition in chemistry climate models. Atmos. Chem. Phys. 15, 11789–11805. https://doi.org/10.5194/acp-15-11789-2015

Strode, S.A., Pawson, S., 2013. Detection of carbon monoxide trends in the presence of

1077 interannual variability. J. Geophys. Res. Atmos. 118, 12,257-12,273.
1078 https://doi.org/10.1002/2013JD020258
1079 Tie, X.X., Jim Kao, C.Y., Mroz, E.J., 1992. Net yield of OH, CO, and O3 from the oxidation
1080 of atmospheric methane. Atmos. Environ. Part A, Gen. Top. 26, 125–136.
1081 https://doi.org/10.1016/0960-1686(92)90265-M
1082 van der Werf, G.R., Randerson, J.T., Giglio, L., Collatz, G.J., Mu, M., Kasibhatla, P.S.,
1083 Morton, D.C., DeFries, R.S., Jin, Y., van Leeuwen, T.T., 2010. Global fire emissions
1084 and the contribution of deforestation, savanna, forest, agricultural, and peat fires (1997–
1085 2009). Atmos. Chem. Phys. 10, 11707–11735. https://doi.org/10.5194/acp-10-11707-
1086 2010
1087 Wang, T., Wei, X.L., Ding, A.J., Poon, C.N., Lam, K.S., Li, Y.S., Chan, L.Y., Anson, M.,
1088 2009. Increasing surface ozone concentrations in the background atmosphere of
1089 Southern China, 1994-2007. Atmos. Chem. Phys. 9, 6217–6227.
1090 https://doi.org/10.5194/acp-9-6217-2009
1091 Wang, T., Wong, H.L.A., Tang, J., Ding, A., Wu, W.S., Zhang, X.C., 2006. On the origin of
1092 surface ozone and reactive nitrogen observed at a remote mountain site in the
1093 northeastern Qinghai-Tibetan Plateau, western China. J. Geophys. Res. Atmos. 111.
1094 https://doi.org/10.1029/2005JD006527
1095 Warner, J., Carminati, F., Wei, Z., Lahoz, W., Attié, J.-L., 2013. Tropospheric carbon
1096 monoxide variability from AIRS under clear and cloudy conditions. Atmos. Chem. Phys.
1097 13, 12469–12479. https://doi.org/10.5194/acp-13-12469-2013
1098 WHO, 1999. Environmental health criteria 213 carbon monoxide (second edition), in:
1099 Environmental Health Criteria. pp. 349–410.
1100 WMO-GAW, 2010. GAW Report No . 192 Guidelines for the Measurement of Atmospheric
1101 Carbon Monoxide. World Meteorol. Organ. Glob. Atmos. Watch 41.

Worden, H.M., Deeter, M.N., Frankenberg, C., George, M., Nichitiu, F., Worden, J., Aben, I., Bowman, K.W., Clerbaux, C., Coheur, P.F., De Laat, A.T.J., Detweiler, R., Drummond, J.R., Edwards, D.P., Gille, J.C., Hurtmans, D., Luo, M., Martínez-Alonso, S., Massie, S., Pfister, G., Warner, J.X., 2013. Decadal record of satellite carbon monoxide observations. Atmos. Chem. Phys. 13, 837–850. https://doi.org/10.5194/acp-13-837-2013

Wu, Y., Han, Y., Voulgarakis, A., Wang, T., Li, M., Wang, Y., Xie, M., Zhuang, B., Li, S., 2017. An agricultural biomass burning episode in eastern China: Transport, optical properties, and impacts on regional air quality. J. Geophys. Res. Atmos. 122, 2304–2324. https://doi.org/https://doi.org/10.1002/2016JD025319

Xia, Y., Zhao, Y., Nielsen, C.P., 2016. Benefits of China's efforts in gaseous pollutant control indicated by the bottom-up emissions and satellite observations 2000–2014. Atmos. Environ. 136, 43–53. https://doi.org/https://doi.org/10.1016/j.atmosenv.2016.04.013

Xiong, H., Lin, Y., Liu, S., Zang, K., Chen, Y., Liu, P., Liang, M., Jiang, K., Qing, X., Qiu, S., Hong, H., Li, J., Fang, S., 2022. Variations of atmospheric CO concentration from 2004 to 2019 at the Mt. Waliguan station in China. Atmos. Res. 271, 106060. https://doi.org/https://doi.org/10.1016/j.atmosres.2022.106060

Yang, X., Zhao, C., Yang, Y., Yan, X., Fan, H., 2021. Statistical aerosol properties associated with fire events from 2002 to 2019 and a case analysis in 2019 over Australia. Atmos. Chem. Phys. 21, 3833–3853. https://doi.org/10.5194/acp-21-3833-2021

Yashiro, H., Sugawara, S., Sudo, K., Aoki, S., Nakazawa, T., 2009. Temporal and spatial variations of carbon monoxide over the western part of the Pacific Ocean. J. Geophys. Res. Atmos. 114, 1–17. https://doi.org/10.1029/2008JD010876

Yin, Y., Bloom, A.A., Worden, J., Saatchi, S., Yang, Y., Williams, M., Liu, J., Jiang, Z.,

1127 Worden, H., Bowman, K., Frankenberg, C., Schimel, D., 2020. Fire decline in dry
1128 tropical ecosystems enhances decadal land carbon sink. Nat. Commun. 11, 1900.
1129 https://doi.org/10.1038/s41467-020-15852-2
1130 Yin, Y, Chevallier, F., Ciais, P., Broquet, G., Fortems-Cheiney, A., Pison, I., Saunois, M.,
1131 2015. Decadal trends in global CO emissions as seen by MOPITT. Atmos. Chem. Phys.
1132 15, 13433–13451. https://doi.org/10.5194/acp-15-13433-2015
1133 Yin, Y., Chevallier, F., Ciais, P., Broquet, G., Fortems-Cheiney, A., Pison, I., Saunois, M.,
1134 2015. Decadal trends in global CO emissions as seen by MOPITT. Atmos. Chem. Phys.
1135 15, 13433–13451. https://doi.org/10.5194/acp-15-13433-2015
1136 Yoon, J., Pozzer, A., 2014. Model-simulated trend of surface carbon monoxide for the 2001-
1137 2010 decade. Atmos. Chem. Phys. 14, 10465–10482. https://doi.org/10.5194/acp-14-
1138 10465-2014
1139 Yumimoto, K., Uno, I., Itahashi, S., 2014. Long-term inverse modeling of Chinese CO
1140 emission from satellite observations. Environ. Pollut. 195, 308–318.
1141 https://doi.org/https://doi.org/10.1016/j.envpol.2014.07.026
1142 Zellweger, C., Hüglin, C., Klausen, J., Steinbacher, M., Vollmer, M., Buchmann, B., 2009.
1143 Inter-comparison of four different carbon monoxide measurement techniques and
1144 evaluation of the long-term carbon monoxide time series of Jungfraujoch. Atmos. Chem.
1145 Phys. 9, 3491–3503. https://doi.org/10.5194/acp-9-3491-2009
1146 Zhang, F., Zhou, L.X., Novelli, P.C., Worthy, D.E.J., Zellweger, C., Klausen, J., Ernst, M.,
1147 Steinbacher, M., Cai, Y.X., Xu, L., Fang, S.X., Yao, B., 2011. Evaluation of in situ
1148 measurements of atmospheric carbon monoxide at Mount Waliguan, China. Atmos.
1149 Chem. Phys. 11, 5195–5206. https://doi.org/10.5194/acp-11-5195-2011
1150 Zhang, X., Liu, J., Han, H., Zhang, Y., Jiang, Z., Wang, H., Meng, L., Li, Y.C., Liu, Y., 2020.
1151 Satellite-Observed Variations and Trends in Carbon Monoxide over Asia and Their

1152 Sensitivities to Biomass Burning. Remote Sens. 12. https://doi.org/10.3390/rs12050830
1153 Zheng, Bo, Chevallier, F., Ciais, P., Yin, Y., Deeter, M.N., Worden, H.M., Wang, Y., Zhang,
1154 Q., He, K., 2018. Rapid decline in carbon monoxide emissions and export from East
1155 Asia between years 2005 and 2016. Environ. Res. Lett. 13. https://doi.org/10.1088/1748-
1156 9326/aab2b3
1157 Zheng, B., Chevallier, F., Yin, Y., Ciais, P., Fortems-Cheiney, A., Deeter, M.N., Parker, R.J.,
1158 Wang, Y., Worden, H.M., Zhao, Y., 2019. Global atmospheric carbon monoxide budget
1159 2000-2017 inferred from multi-species atmospheric inversions. Earth Syst. Sci. Data 11,
1160 1411–1436. https://doi.org/10.5194/essd-11-1411-2019
1161 Zheng, B, Tong, D., Li, M., Liu, F., Hong, C., Geng, G., Li, H., Li, X., Peng, L., Qi, J., Yan,
1162 L., Zhang, Y., Zhao, H., Zheng, Y., He, K., Zhang, Q., 2018. Trends in China's
1163 anthropogenic emissions since 2010 as the consequence of clean air actions. Atmos.
1164 Chem. Phys. 18, 14095–14111. https://doi.org/10.5194/acp-18-14095-2018
1165 Alvarado, M.J., Lonsdale, C.R., Yokelson, R.J., Akagi, S.K., Coe, H., Craven, J.S., Fischer, E.
1166 V, McMeeking, G.R., Seinfeld, J.H., Soni, T., Taylor, J.W., Weise, D.R., Wold, C.E.,
1167 2015. Investigating the links between ozone and organic aerosol chemistry in a biomass
1168 burning plume from a prescribed fire in California chaparral. Atmos. Chem. Phys. 15,
1169 6667–6688. https://doi.org/10.5194/acp-15-6667-2015
1170 Coggon, M.M., Lim, C.Y., Koss, A.R., Sekimoto, K., Yuan, B., Gilman, J.B., Hagan, D.H.,
1171 Selimovic, V., Zarzana, K.J., Brown, S.S., Roberts, J.M., Müller, M., Yokelson, R.,
1172 Wisthaler, A., Krechmer, J.E., Jimenez, J.L., Cappa, C., Kroll, J.H., de Gouw, J.,
1173 Warneke, C., 2019. OH chemistry of non-methane organic gases (NMOGs) emitted
1174 from laboratory and ambient biomass burning smoke: evaluating the influence of furans
1175 and oxygenated aromatics on ozone and secondary NMOG formation. Atmos. Chem.
1176 Phys. 19, 14875–14899. https://doi.org/10.5194/acp-19-14875-2019

Crotwell A., H. Lee, M. Steinbacher (eds), 20th WMO/IAEA Meeting on Carbon Dioxide, Other Greenhouse Gases and Related Measurement Techniques (GGMT-2019), pp 151, World Meteorological Organization (WMO), GAW Report No. 255, 2020. https://library.wmo.int/doc_num.php?explnum_id=10353.

Crutzen, P.J., Andreae, M.O., 1990. Biomass Burning in the Tropics: Impact on Atmospheric Chemistry and Biogeochemical Cycles. Science (80-.). 250, 1669–1678. https://doi.org/10.1126/science.250.4988.1669

Jaffe, D.A., Wigder, N.L., 2012. Ozone production from wildfires: A critical review. Atmos. Environ. 51, 1–10. https://doi.org/https://doi.org/10.1016/j.atmosenv.2011.11.063

Matsueda, H., R. R. Buchholz, K. Ishijima, H. M. Worden, D. Hammerling, and T. Machida, 2019: Interannual variation of upper tropospheric CO over the western Pacific linked with Indonesian fires. SOLA, 15, 205−210, doi:10.2151/sola.2019037

Müller, M., Anderson, B.E., Beyersdorf, A.J., Crawford, J.H., Diskin, G.S., Eichler, P., Fried, A., Keutsch, F.N., Mikoviny, T., Thornhill, K.L., Walega, J.G., Weinheimer, A.J., Yang, M., Yokelson, R.J., Wisthaler, A., 2016. In situ measurements and modeling of reactive trace gases in a small biomass burning plume. Atmos. Chem. Phys. 16, 3813–3824. https://doi.org/10.5194/acp-16-3813-2016

Osman, M. K., Tarasick, D. W., Liu, J., Moeini, O., Thouret, V., Fioletov, V. E., Parrington, M., and Nédélec, P.: Carbon monoxide climatology derived from the trajectory mapping of global MOZAIC-IAGOS data, Atmos. Chem. Phys., 16, 10263–10282, https://doi.org/10.5194/acp-16-10263-2016, 2016.

Tang, Y., Carmichael, G.R., Woo, J.-H., Thongboonchoo, N., Kurata, G., Uno, I., Streets, D.G., Blake, D.R., Weber, R.J., Talbot, R.W., Kondo, Y., Singh, H.B., Wang, T., 2003. Influences of biomass burning during the Transport and Chemical Evolution Over the

Pacific (TRACE-P) experiment identified by the regional chemical transport model. J. Geophys. Res. Atmos. 108. https://doi.org/https://doi.org/10.1029/2002JD003110

Zhu, B., Huang, X.-F., Xia, S.-Y., Lin, L.-L., Cheng, Y., He, L.-Y., 2021. Biomass-burning emissions could significantly enhance the atmospheric oxidizing capacity in continental air pollution. Environ. Pollut. 285, 117523. https://doi.org/https://doi.org/10.1016/j.envpol.2021.117523

List of Figures

Figure 1. Spatial coverage of stations selected for this analysis from WDCGG database (http://ds.data.jma.go.jp/gmd/wdcgg/). The sites are operated by NOAA and JMA. See Table S1 for full names and coordinates of the stations.

Figure 2. Data coverage for each site selected for this analysis from WDCGG database (http://ds.data.jma.go.jp/gmd/wdcgg/). Left panel is the data availability of original monthly dataset having some missing data points for few sites. Right panel is the final monthly data availability after curve fitting.

Figure 3. Spatial distribution of long-term trends in atmospheric CO during 1991-2020. There is an overall declining trend in CO in last 3 decade. The significance of CO trends as p-values can be found in Figure S1. There are few sites with insignificant confidence interval. However, these sites are kept in the analysis for their critical location on world map.

Figure 4. Time series of CO mixing ratios from WDCGG for the 3 broad latitude bands, of 75^{o}N - 23.5^{o}N, 23.5^{o}N - 23.5^{o}S, and 23.5^{o}S - 70^{o}S (panels a-c). The corresponding regional total CO emissions derived from EDGAR v6.0 are also shown (panels d-f). ENSO-events are also shown (moderate La Nina: 2007-08, 2010-11; very strong El Nino: 1997-98, 2015-16; moderate El Nino: 2002-03, 2009-10)

Figure 5. Latitudinal gradient of CO trends as observed at 49 sites. A dominancy of NH sites is observed latitudinally, with continental sites (Δ-marker) contributing higher CO (ppb) than the sites with marine background (□- marker). The colored circle inside each marker provides the information of the length of time series data (in years) available for each site.

Figure 6. 5 regional clusters representing average long-term trend of each cluster. Each cluster is grouped according on the closeness to centroid value of long-term trend, latitude and longitude representing each region. A set of European + north Atlantic sites; Cluster-1 shows most negative trends of all groups and contributing more to negative trends in NH.

Figure 7. Decadal decouple of CO trends into 1990s, 2000s and 2010s. Representation of non-uniform decrease in all decades mostly in SH whereas a continuous decrease in NH. But a positive inter-decadal trend difference (δ-trend) reveals the weakening of decreasing trends of CO in 2010s w.r.t to previous decades.

Figure 8. Spatial representation of relative decadal changes in growth rate in 2011-2020 decade with respect to 2001-2010. δ-Trend is the difference of growth rates in 2010s and 2000s. +ve difference in δ-Trend meaning the magnitude of negative growth rates in CO has been reduced or have become positive and vice versa in the recent decade. Red/brown markers are the spatially distributed 39 out of 49 sites depicting CO is decreasing with slower rate or have positively increasing trend during 2010s with respect to 2000s.

Figure 9. Seasonal cycles of CO at 3 sites each in the NH (top row) and SH (bottom row). Blue to red color correspond to the seasonal cycles with high and low annual CO mixing ratio, respectively, during the period of the 1991 to 2020.

Figure 10. Latitudinal gradient of CO seasonal (DJF, MAM, JJA, SON) trends and overall decrease in CO mixing ratio during 1991-2020. Extreme negative trends in 40 ^{o}N -50 ^{o}N resulted in maximum CO (ppb) decrease over these sites (> -30 ppb) in all seasons. SON season dominated an average reduction of ~ 3.5 – 3.7 ppb in SH.

1251 **Figure 11.** A contrasting positive trend over South-Asian sites during 1991-2020 in JJA
1252 season. 5 out of 9 sites had positive trends unlike other seasons.